

# Characterising self-resonance during preheating



Yanfang Angela Piao Xue

Department of Physics  
The University of Auckland

Supervisor: Professor Richard Easther

A dissertation submitted in partial fulfilment of the requirements for the degree of BSc(Hons)  
in Physics, The University of Auckland, 2021.

# Abstract

The Monodromy model provides a well-motivated and well-studied potential exhibiting self-resonance during the preheating period after inflation in the early universe. This project aims to study a particular Monodromy model introduced by Amin et al. and its resonance structure to assess how the quartic and sixth order Taylor expansion terms contribute to self-resonance of inflaton perturbations. I find that the forth and sixth order approximations are usually not effective at reproducing the finer details of the resonant structures produced by the Monodromy model, hence higher order terms are needed. For higher values of one key parameter, the sixth order approximation captures the resonant structure of the Monodromy model well, and may provide sufficient information about the Monodromy model in the context of preheating.

# Contents

<b>1</b>	<b>Introduction</b>	<b>3</b>
1.1	Hot Big Bang and Inflation . . . . .	3
1.2	Reheating and Preheating . . . . .	3
<b>2</b>	<b>Mathematical Background</b>	<b>5</b>
2.1	Inflation in the FRW Universe . . . . .	5
2.1.1	Slow-roll Inflation . . . . .	6
2.2	Preheating through Self-Resonance . . . . .	6
2.2.1	Non-expanding Universe . . . . .	6
2.2.2	Expanding Universe . . . . .	7
2.3	Potential Functions . . . . .	7
<b>3</b>	<b>Methods</b>	<b>9</b>
3.1	Overview . . . . .	9
3.2	Floquet Theory . . . . .	9
3.2.1	Finding the Floquet Exponent . . . . .	10
3.2.2	Numerical Integration . . . . .	10
3.3	Quartic Potential . . . . .	11
3.3.1	Solving for the Background Inflaton Field . . . . .	11
3.3.2	Integrate for Inflaton Perturbations . . . . .	13
3.3.3	Mathieu Stability Charts . . . . .	13
<b>4</b>	<b>The Monodromy Potential</b>	<b>16</b>
4.1	Summary of the Monodromy Potential . . . . .	16
4.2	The Quartic and Sixth Order Terms . . . . .	17
4.3	Results from Mathieu Equation . . . . .	20
4.4	Accuracy of Results . . . . .	24
4.4.1	Accuracy of the Differential Equation as a Mathieu Equation . . . . .	24
<b>5</b>	<b>Conclusion</b>	<b>29</b>
<b>A</b>	<b>More Comparisons</b>	<b>30</b>
<b>B</b>	<b><math>\phi^6</math> Potential</b>	<b>34</b>

# Chapter 1

## Introduction

### 1.1 Hot Big Bang and Inflation

The Hot Big Bang theory accurately predicts and explains many cosmological phenomena. Although this theory remains (and probably will remain) unchallenged, it is not complete. Particularly, observations of today's universe require assumptions of very fine tuned and improbable initial conditions in the early universe; these problems are known as the flatness and horizon problems; (these problems are more thoroughly discussed in [1, 2, 3, 4]). To resolve the fine tuning issues of the standard Big Bang theory inflation was posed as a possible solution [4].

Cosmological inflation posits that the very early universe was expanding at an accelerating rate. It is believed to have occurred within a time of  $\sim 10^{-35}$  seconds and observational constraints require that the universe grew by at least a factor of  $e^N$ ,  $N \sim 60$  e-folds during this time. The mechanism which propels the universe to expand at such a rate is attributed to a scalar field called the inflaton field<sup>1</sup> — this theory gained confidence after the discovery of the Higgs field in 2012, the first observed scalar field. The inflaton field maintains an almost constant energy density during inflation, resembling a cosmological constant and driving the almost exponential expansion of the universe. Inflation ends with the energy density of the inflaton field dropping to a vacuum state resulting in a very dense, very cool universe dominated by the inflaton condensate. The post inflationary universe is also very homogeneous, providing a solution to the horizon problem.

### 1.2 Reheating and Preheating

While inflation satisfactorily resolves problems with the standard Big Bang theory, the state of the universe at the end of inflation necessarily disagrees with the state at the beginning of the Big Bang universe. The very early universe as we understand it begins with quarks condensing into protons and neutrons, followed by the creation of light nuclei through nucleosynthesis, all while the universe is hot and radiation dominated. Additionally, the early universe, while homogeneous on large scales, must also be somewhat inhomogeneous on small scales for structures to form via self gravitation. This disagreement may be bridged by the phenomena dubbed reheating and preheating.

Reheating is the process whereby the cool, inflaton condensate dominated post inflationary universe is heated and thermalises into a hot radiation dominated universe. Preheating is a process wherein there is an explosive growth in perturbations of the inflaton field through parametric resonance, creating particles through the decay of the inflaton at an exponential rate. The

---

<sup>1</sup>It is unknown exactly what the inflaton particle is, nevertheless proposing its existence is very useful.

growth in inflaton perturbations through preheating also lead to very small local wavelength inhomogeneities and transients in the universe.

The specific dynamics of the creation of other particles during preheating is model dependent. While particle production can be achieved with the inflaton field coupling to other fields, the inflaton perturbations interacting with its average, non perturbed motion may also lead to copious particle productions. This latter process is called self-resonance, which this dissertation focuses on.

## Chapter 2

# Mathematical Background

### 2.1 Inflation in the FRW Universe

The units used in this project are  $c = \hbar = 1$ ; additionally  $G = 1/8\pi$ . The Planck mass is  $m_{\text{Pl}} = 1/\sqrt{G}$  and  $M_{\text{Pl}} = m_{\text{Pl}}\sqrt{G} = 1$  is the reduced Planck mass. We assume a universe that is homogeneous, isotropic and expanding on large scales, and thus use the Friedmann-Robertson-Walker (FRW) metric. The equations of motion derived from this metric are

$$\left(\frac{\dot{a}}{a}\right)^2 = H^2 = \frac{8\pi}{3m_{\text{Pl}}^2}\rho - \frac{\kappa}{a^2}, \quad (2.1)$$

$$\dot{\rho} + 3H(\rho + p) = 0, \quad (2.2)$$

which are the Friedmann and fluid equations respectively. The Friedmann equation describes the expanding universe with curvature  $\kappa$ ,  $\kappa = 0$  representing a flat universe. The fluid equation describes how materials in the universe respond to an expanding universe. The energy density and the pressure of any material in the universe are denoted  $\rho$  and  $p$  respectively and may be related by the equation of state parameter  $w$  defined by the equation of state;

$$p = w\rho. \quad (2.3)$$

The Hubble parameter defined by  $H = \frac{\dot{a}}{a}$  describes the rate of expansion of the universe where  $a$  is the scale factor which relates the physical size of the universe to its comoving size. Overdots denote derivatives with respect to coordinate time. We can combine the Friedmann and fluid equations to obtain a third equation;

$$\frac{\ddot{a}}{a} = -\frac{4\pi}{3m_{\text{Pl}}^2}(\rho + 3p) \quad (2.4)$$

which is the acceleration equation. For a scalar field, denoted  $\phi$ , the specific dynamics of the universe is determined by its potential  $V(\phi)$  which is its only adjustable function. The energy density and pressure of the field are potential dependent

$$\rho = \frac{1}{2}\dot{\phi}^2 + V(\phi), \quad p = \frac{1}{2}\dot{\phi}^2 - V(\phi) \quad (2.5)$$

where we ignore the local inhomogeneities of the field. The accompanying Klein-Gordon equation, which can be derived from the fluid equation is

$$\ddot{\phi} + 3H\dot{\phi} + \frac{\partial V}{\partial \phi} = 0. \quad (2.6)$$

and the Friedmann equation

$$H^2 = \frac{8\pi}{3m_{\text{Pl}}^2} \left( \frac{1}{2}\dot{\phi}^2 + V(\phi) \right) \quad (2.7)$$

where  $\kappa$  rapidly approaches 0 as the universe becomes flat during inflation and is hence not included in what follows.

### 2.1.1 Slow-roll Inflation

In the early universe,  $\ddot{a} > 0$  defines the inflationary period. Solving the acceleration equation with this condition requires that  $w < -1/3$  during the inflationary period, or equivalently  $\dot{\phi}^2 < V(\phi)$ . Taking the extreme of this inequality,  $\dot{\phi}^2 \ll V(\phi)$ , characterises the slow-roll approximation. We may define a slow roll parameter  $\epsilon$

$$\frac{\ddot{a}}{a} = H^2(1 - \epsilon), \quad \epsilon(\phi) \equiv \frac{3}{2} \left( \frac{p}{\rho} + 1 \right) \quad (2.8)$$

where

$$\epsilon(\phi) = \frac{m_{\text{Pl}}^2}{16\pi} \left( \frac{V'(\phi)}{V(\phi)} \right)^2 \quad (2.9)$$

in the slow-roll limit. This slow roll parameter describes the slope of an inflaton potential. In the slow-roll approximation, the requirement  $\dot{\phi}^2 \ll V(\phi)$  translates to  $\epsilon \ll 1$  during inflation, which describes a potential which is very flat and  $\epsilon(\phi_{\text{end}}) = 1$  marks the end of inflation. After inflation, the inflaton field drops into a potential well and oscillates about the potential minima, hence starting preheating period of the universe.

## 2.2 Preheating through Self-Resonance

The slow roll conditions expire and inflation ends when the inflaton potential reaches a sufficiently small value. A mechanism wherein the inflaton condensate decays through self-resonance is driven by perturbations of the inflaton field interacting with the background inflaton motion as it oscillates about the minima of its potential near its vacuum energy. To understand this, consider the Klein-Gordon equation, this time including the perturbations in the inflaton field;

$$\ddot{\phi} + 3H\dot{\phi} - \frac{\nabla^2}{a^2}\phi + \frac{\partial V}{\partial\phi} = 0. \quad (2.10)$$

The dynamics of the inflaton perturbations will be investigated quantitatively for a non-expanding universe.

### 2.2.1 Non-expanding Universe

We ignore the expansion terms in this equation by setting  $H = 0$  and  $a = 1$ , resulting in the equation of motion

$$\ddot{\phi} - \nabla^2\phi + \frac{\partial V}{\partial\phi} = 0. \quad (2.11)$$

Consider decomposing the inflaton field into a small perturbation  $\delta\phi(t, \mathbf{x})$  on top its homogeneous background motion  $\bar{\phi}(t)$ ;

$$\phi(t, \mathbf{x}) = \bar{\phi}(t) + \delta\phi(t, \mathbf{x}), \quad \delta\phi(t, \mathbf{x}) = \int_{-\infty}^{\infty} \delta\phi_k(t)e^{i\mathbf{k}\cdot\mathbf{x}} dk \quad (2.12)$$

where we can solve for one comoving wave mode  $k$  at a time. Solving for equation 2.11 with a single  $k$  mode results in the equation of motion

$$\ddot{\phi} + V'(\bar{\phi}) + \delta\ddot{\phi}_k e^{ik \cdot x} + [k^2 + V''(\bar{\phi})]\delta\phi_k e^{ik \cdot x} = 0 \quad (2.13)$$

where ' denotes derivative with respect to  $\phi$  and all higher order terms of  $\delta\phi_k$  are ignored. This equation is solved if

$$\ddot{\phi} + V'(\bar{\phi}) = 0, \quad (2.14)$$

$$\delta\ddot{\phi}_k + [k^2 + V''(\bar{\phi})]\delta\phi_k = 0 \quad (2.15)$$

which are the basic equations of motion.

### 2.2.2 Expanding Universe

Reintroducing the expansion terms into equation 2.11 results in an effective damping term  $3H\dot{\phi}$  on the amplitude of oscillations of the background field and perturbations of  $\phi$ . Additionally, the physical wave number  $\frac{k}{a}$  decreases during reheating. In general, the expansion of the universe directly following the inflationary period results in a rapid decrease in the amplitude of inflaton oscillations and physical wave number. The rate of expansion of the universe decreases with time after inflation.

From here on, I shall drop the bar on the background inflaton field  $\bar{\phi} \rightarrow \phi$  for cleaner presentation and will refer to the full  $\bar{\phi}(t) + \delta\phi(t, \mathbf{x})$  inflaton field explicitly as  $\phi(t) + \delta\phi(t, \mathbf{x})$ .

## 2.3 Potential Functions

In a single field scalar theory, the qualitative features of reheating are dependent solely on the shape of the inflaton potential. A well-motivated and well-studied potential is the Monodromy potential. Specific forms of this potential vary but I shall look at the following from [5]

$$V(\phi) = \frac{m^2 M^2}{2\alpha} \left[ \left( 1 + \frac{\phi^2}{M^2} \right)^\alpha - 1 \right], \quad (2.16)$$

$$V(\phi) \sim \begin{cases} \phi^{2\alpha}, & |\phi| \gg M \\ \phi^2, & |\phi| \ll M \end{cases}. \quad (2.17)$$

This potential satisfies the slow-roll condition at large  $\phi$ . The special case of  $\alpha = 1$  retrieves the harmonic potential which trivially exhibits no self-resonance. To investigate how much the fourth order and sixth order terms in  $\phi$  contribute to the resonance of the inflaton field we may Taylor expand the Monodromy potential up to the fourth and sixth order about its minima;

$$V(\phi) = \frac{1}{2} m^2 \phi^2 + \frac{m^2(\alpha - 1)}{4M^2} \phi^4 + \dots \quad (2.18)$$

or

$$V_4(\phi) = m^2 \left( \frac{1}{2} \phi^2 + \frac{\lambda}{4m^2} \phi^4 \right) \quad (2.19)$$

$$V_6(\phi) = m^2 \left( \frac{1}{2} \phi^2 + \frac{\lambda}{4m^2} \phi^4 + \frac{g}{6m^2} \phi^6 \right) \quad (2.20)$$

where

$$\frac{\lambda}{m^2} = \frac{\alpha - 1}{M^2}, \quad \frac{g}{m^2} = \frac{(\alpha - 1)(\alpha - 2)}{2M^4}. \quad (2.21)$$

I shall keep  $m^2 = 1$  constant as it does not affect the qualitative dynamics of the problem.

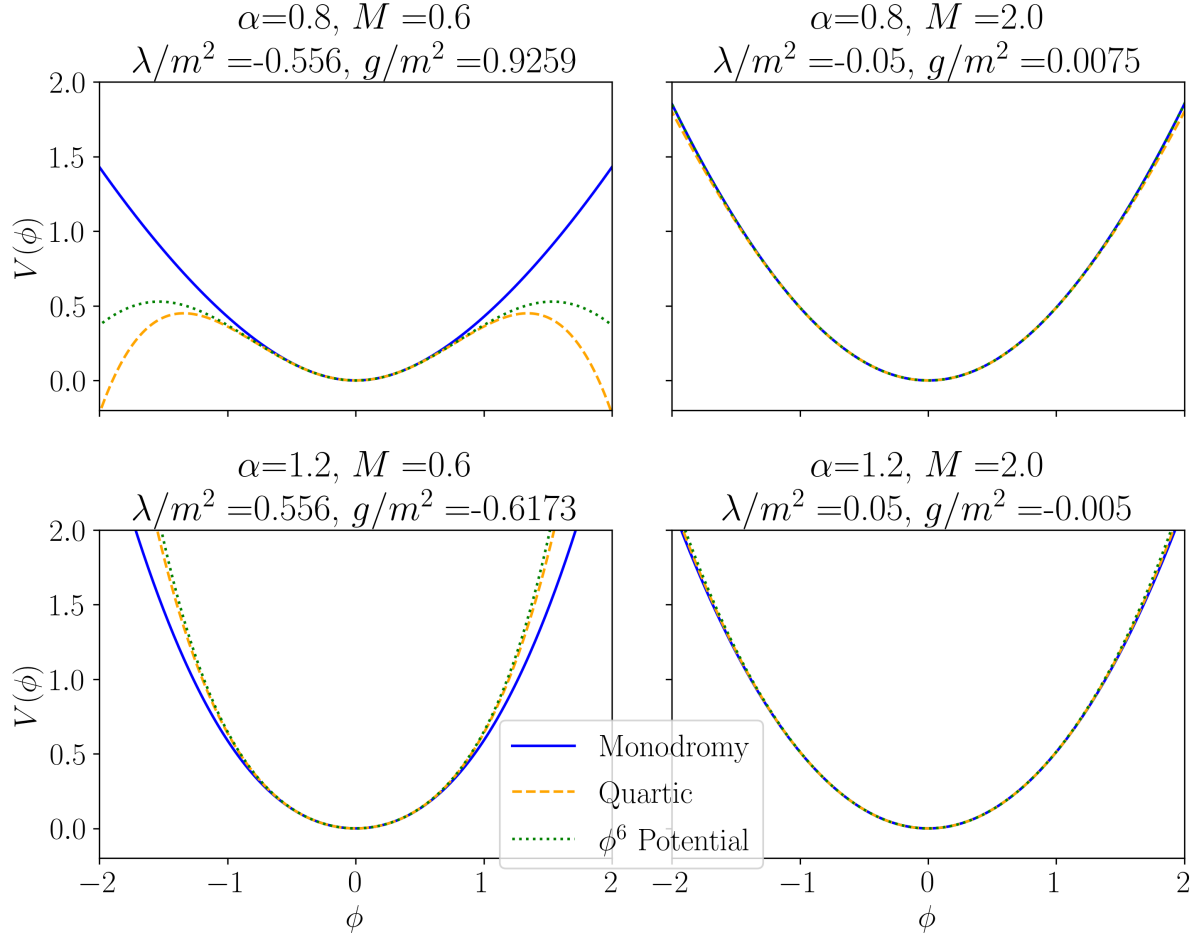


Figure 2.1: The Monodromy,  $V_4(\phi)$  and  $V_6(\phi)$  potentials according to equations 2.16, 2.19 and 2.20 respectively with  $\lambda/m^2$ ,  $g/m^2$  defined according equation 2.21. Since we are only concerned with the dynamics after inflation, we need only to worry about convergence of expanded potentials near the minima.

# Chapter 3

## Methods

### 3.1 Overview

To understand whether the dynamics of the inflaton field results in an explosive growth of inflaton perturbations, we need to solve equation 2.15. The only parameters that affect its dynamics are the wave number  $k$  and  $V''(\phi(t))$  which contribute to its forcing term. In principle,  $k \in (0, \infty)$ , however the interesting dynamics occur for low  $k$ , so we will focus on this range. We find  $V''(\phi(t))$  by solving for the background inflaton field through equation 2.14. In general, equation 2.14 is nonlinear, hence its solution is initial condition dependent. The initial conditions used are  $\phi(0) = \phi_0$  and  $\dot{\phi}(0) = 0$  where  $\phi_0$  is sampled between 0 and  $\sim \phi_{\text{end}}$  and  $\phi_{\text{end}}$  is given usually by solving  $\epsilon(\phi_{\text{end}}) = 1$  determined by the potential of interest. The solution for  $\phi(t)$  gives us  $V''(\phi(t))$ . For a given potential, the parameters that affect the dynamics of the inflaton perturbations boil down to just  $k$  and  $\phi_0$  — the growth of the inflaton perturbations in a single period plotted on  $k$ - $\phi_0$  axes is a called stability chart. For the  $V_4(\phi)$  and  $V_6(\phi)$  potentials, there are cases where solving  $\epsilon(\phi_{\text{end}}) = 1$  produces  $\phi_{\text{end}}$  which are too large to consider; either in the context of Taylor approximating the Monodromy potential about its minima, or where  $\phi_{\text{end}}$  falls out of the potential well of  $V_4(\phi)$  or  $V_6(\phi)$ . In these cases, I artificially reduced  $\phi_{\text{end}}$  to the scale of  $\phi_{\text{end}}$  found with the corresponding Monodromy potential.

Generally, the system of equations 2.14 and 2.15 will be numerically integrated together as a system of four single order differential equations. However, for the case of the quartic potential in equation 2.19, there exists exact solutions to the background inflaton potential and an analytic approximation for the dynamics of the inflaton perturbations, both of which decrease numerical error. The quartic potential will be covered separately in section 3.3.

### 3.2 Floquet Theory

The background inflaton field in the non-expanding universe is periodic, hence the equation of motion for the inflaton perturbations equation will have a periodic forcing term. Floquet theory [6, 7] tells us for a such a differential equation with a periodic forcing term, there exists solutions for  $\delta\phi_k$  of the form

$$\delta\phi_k(t) = \mathcal{P}_+(t)e^{\mu_k t} + \mathcal{P}_-(t)e^{-\mu_k t} \quad (3.1)$$

where  $\mathcal{P}_{\pm}$  are periodic functions. Hence, it is the *Floquet exponent*  $\mu_k \in \mathbb{C}$  which determines the growth of the inflaton perturbations; specifically  $\delta\phi_k$  is stable and doesn't grow if and only if  $\Re(\mu_k) = 0$ .

### 3.2.1 Finding the Floquet Exponent

Provided we can solve for the oscillating background field  $\phi(t)$ , we may treat the system as a 2 dimensional differential equation such that

$$\begin{pmatrix} \delta\ddot{\phi}_k \\ \delta\dot{\phi}_k \end{pmatrix} = \begin{pmatrix} 0 & 1 \\ -[k^2 + V''(\phi)] & 0 \end{pmatrix} \begin{pmatrix} \delta\phi_k \\ \delta\dot{\phi}_k \end{pmatrix} \quad (3.2)$$

where  $A(t) = \begin{pmatrix} 0 & 1 \\ -[k^2 + V''(\phi)] & 0 \end{pmatrix}$  is  $T$ -periodic, and  $T$  is the period of oscillation of the background inflaton field.

For  $j = 1, 2$ , let  $\begin{pmatrix} \delta\phi_k^{(j)}(t) \\ \delta\dot{\phi}_k^{(j)}(t) \end{pmatrix}$  be solutions to equation 3.2. Then define a *fundamental matrix*  $\mathcal{O}(t) = \begin{pmatrix} \delta\phi_k^{(1)}(t) & \delta\phi_k^{(2)}(t) \\ \delta\dot{\phi}_k^{(1)}(t) & \delta\dot{\phi}_k^{(2)}(t) \end{pmatrix}$  which is a solution to the differential equation  $\dot{\mathcal{O}}(t) = A(t)\mathcal{O}(t)$  and has non zero determinant for all  $t$ . Let  $\mathcal{O}(t)$  be the *principal fundamental matrix*, so  $\mathcal{O}(0)$  is the identity matrix.

Floquet theory shows that there exists a constant matrix  $B$  with non zero determinant such that  $\mathcal{O}(t+T) = \mathcal{O}(t)B$  for all  $t$ ; choosing  $t = 0$  yields  $B = \mathcal{O}(T)$ . The eigenvalues of  $B$ ,  $\rho_1$  and  $\rho_2$ , are called the *characteristic multipliers* of the system and  $\mu_1$  and  $\mu_2 \in \mathbb{C}$ , related by  $\rho_j = e^{\mu_j T}, (j = 1, 2)$  are called the *Floquet exponents* of the system. As there are no “friction” terms in the matrix  $A(t)$ , by Abel’s identity [8]  $\det(\mathcal{O}(t)) = 1$  hence  $\det(B) = \rho_1\rho_2 = e^{(\mu_1+\mu_2)T} = 1 \implies \mu_1 + \mu_2 = 0 \implies \mu_1 = -\mu_2$ . The eigenvalues are

$$\mu_{1,2} = \frac{x_1(T) + y_2(T)}{2} \pm \frac{\sqrt{\{x_1(T) - y_2(T)\}^2 + 4x_2(T)y_1(T)}}{2} \quad (3.3)$$

hence the Floquet exponents are

$$\mu_{1,2} = \frac{1}{T} \ln \left[ \frac{\delta\phi_k^{(1)}(T) + \delta\dot{\phi}_k^{(2)}(T)}{2} \pm \frac{\sqrt{\{\delta\phi_k^{(1)}(T) - \delta\dot{\phi}_k^{(2)}(T)\}^2 + 4\delta\phi_k^{(2)}(T)\delta\dot{\phi}_k^{(1)}(T)}}{2} \right] \quad (3.4)$$

using the complex log function. It is only  $\Re(\mu_{1,2})$  which controls the growth of the inflaton perturbations. Since  $\Re(\mu_1) = -\Re(\mu_2)$  by Abel’s identity, and if  $\Re(\mu_{1,2}) \neq 0$ , in late times there will be one dominant term experiencing unstable growth caused by  $|\Re(\mu_{1,2})|$ , hence finding  $|\Re(\mu_{1,2})| \equiv \Re(\mu_k)$  will tell us the stability of inflaton perturbations — post-inflationary perturbations are stable if and only if  $\Re(\mu_k) = 0$ .

### 3.2.2 Numerical Integration

This algorithm is borrowed from Mustafa A. Amin and colleagues [9, 8] and is summarised here. In order to obtain the matrix  $B = \mathcal{O}(T)$ , I numerically integrated the system for  $j = 1, 2$

$$\begin{pmatrix} \dot{\phi}(t) \\ \ddot{\phi}(t) \\ \delta\dot{\phi}_k^{(j)}(t) \\ \ddot{\delta\phi}_k^{(j)}(t) \end{pmatrix} = \begin{pmatrix} 0 & 1 & 0 & 0 \\ -V'(\phi) & 0 & 0 & 0 \\ 0 & 0 & 0 & 1 \\ 0 & 0 & -[k^2 + V''(\phi)] & 0 \end{pmatrix} \begin{pmatrix} \phi(t) \\ \dot{\phi}(t) \\ \delta\phi_k^{(j)}(t) \\ \dot{\delta\phi}_k^{(j)}(t) \end{pmatrix} \quad (3.5)$$

from  $t = 0$  to  $T$  with initial conditions  $(\phi(0), \dot{\phi}(0), \delta\phi_k^{(1)}(0), \dot{\delta\phi}_k^{(1)}(0)) = (\phi_0 \ 0 \ 1 \ 0)$  and  $(\phi(0), \dot{\phi}(0), \delta\phi_k^{(2)}(0), \dot{\delta\phi}_k^{(2)}(0)) = (\phi_0 \ 0 \ 0 \ 1)$ . The period  $T$  is that of the background inflaton oscillations, which can be found with a symmetric potential  $V(\phi)$  through the

integral

$$T = \int_0^{\phi_0} \frac{4d\phi}{\sqrt{2V(\phi_0) - 2V(\phi)}}. \quad (3.6)$$

After obtaining  $\mathcal{O}(T) = \begin{pmatrix} \delta\phi_k^{(1)}(T) & \delta\phi_k^{(2)}(T) \\ \dot{\delta\phi}_k^{(1)}(T) & \dot{\delta\phi}_k^{(2)}(T) \end{pmatrix}$ , I find  $\Re(\mu_k)$  using equation 3.4. Repeating this process for different values of  $k$  and  $\phi_0$  produces a stability chart for inflaton perturbations that is characteristic of different inflaton potentials. Below, figure 3.1 shows sample plots of  $\delta\phi_k(t)$  found through integrating 3.5 for a long time. The different parameters used highlight different qualitative features of the perturbations which can be achieved, depending on the value of the Floquet exponent.

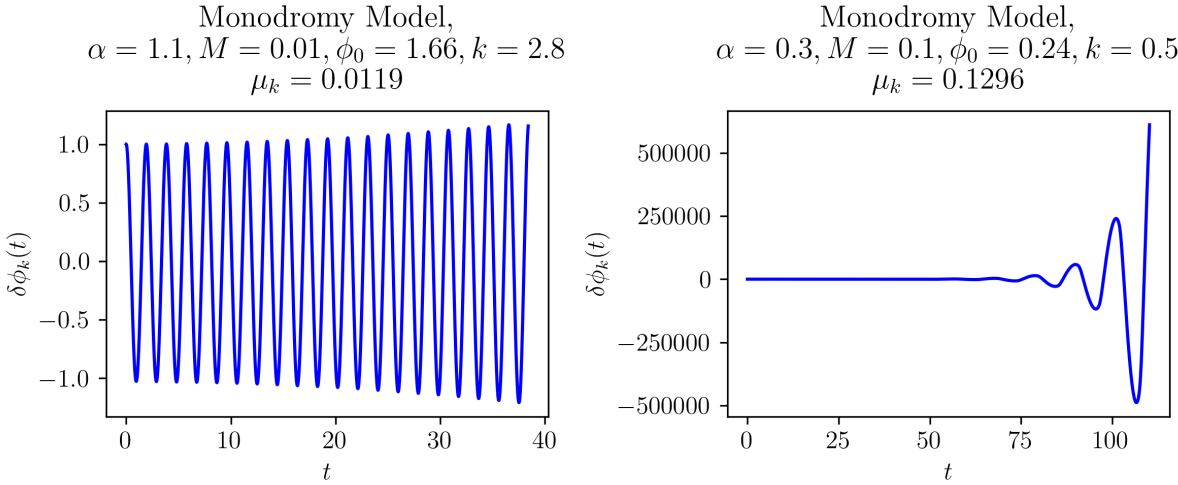


Figure 3.1: Example plots of  $\delta\phi_k(t)$ , showing the growth of perturbations over 10 oscillation periods of the background field  $\phi(t)$ . Greater  $\mu_k$  results in an explosive growth of perturbations; perturbations with smaller  $\mu_k$  are relatively static over the same number of oscillations of the background field.

### 3.3 Quartic Potential

We will examine the quartic potential as an illustrative example and as a test of our methods. The equations of motion for a quartic potential are explicitly

$$\ddot{\phi} + m^2\phi + \lambda\phi^3 = 0 \quad (3.7)$$

$$\ddot{\delta\phi}_k + [k^2 + m^2 + 3\lambda\phi^2]\delta\phi_k = 0 \quad (3.8)$$

The case of  $\lambda = 0$  reduces the inflaton potential a harmonic potential. This potential trivially produces no self-resonance — I will not study this case further.

#### 3.3.1 Solving for the Background Inflaton Field

For  $\lambda \neq 0$ , the system is known as a Duffing equation with analytic solutions in terms of the Jacobi elliptic functions [10]. Setting  $\lambda > 0$  produces periodic solutions of the background field for all values of  $\phi$  and  $\dot{\phi}$ ;  $\lambda < 0$  produces periodic solutions for only a closed region in phase space about  $\phi = \dot{\phi} = 0$  — large  $\phi$  and  $\dot{\phi}$  corresponding to  $\lambda < -m^2/\phi_0^2$  are not of physical

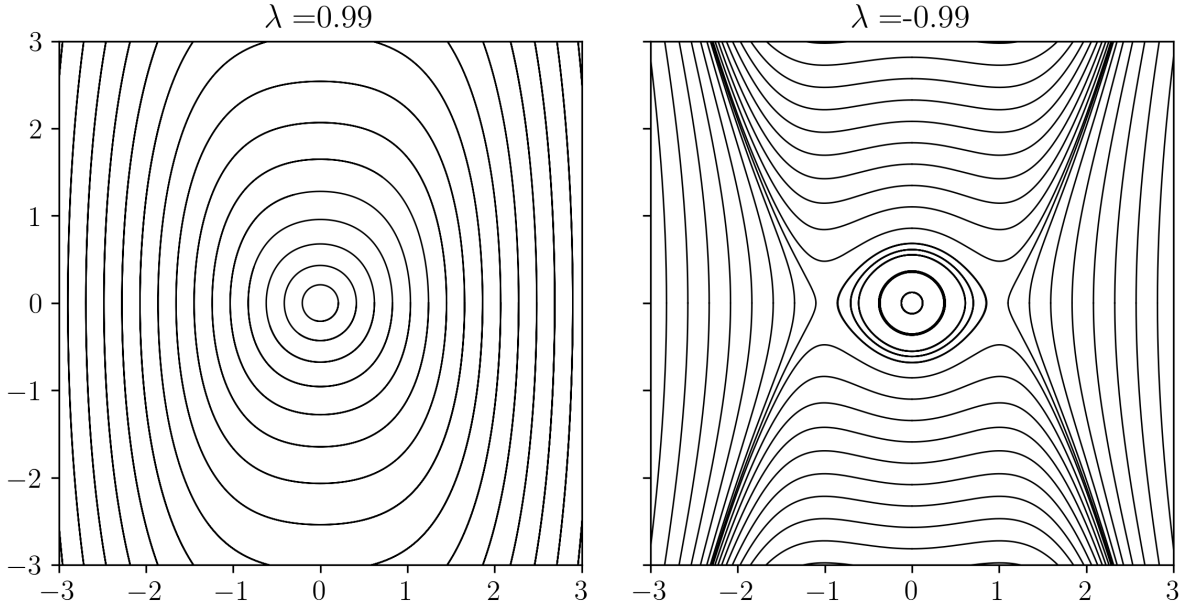


Figure 3.2: The  $\phi\dot{\phi}$  phase space of the equation 3.7.

relevance to us as we are considering only small deviations from the Monodromy model, in addition to  $\phi$  and  $\dot{\phi}$  tending towards  $\pm\infty$ . See figure 3.2.

The solutions are as follows and plotted in figure 3.3, where  $\text{cn}(\cdot, \cdot)$  is a elliptic cosine function;

$$\phi(t) = \phi_0 \text{cn} \left( \sqrt{m^2 + \lambda\phi_0^2} t, \sqrt{\frac{\lambda\phi_0^2}{2(m^2 + \lambda\phi_0^2)}} \right) \quad \text{for } \lambda > 0 \quad (3.9)$$

$$\phi(t) = \phi_0 \text{cd} \left( \sqrt{m^2 + \frac{\lambda\phi_0^2}{2}} t, \sqrt{-\frac{\lambda\phi_0^2}{2m^2 + \lambda\phi_0^2}} \right) \quad \text{for } -m^2/\phi_0^2 < \lambda < 0 \quad (3.10)$$

Samples are plotted in figure 3.3.

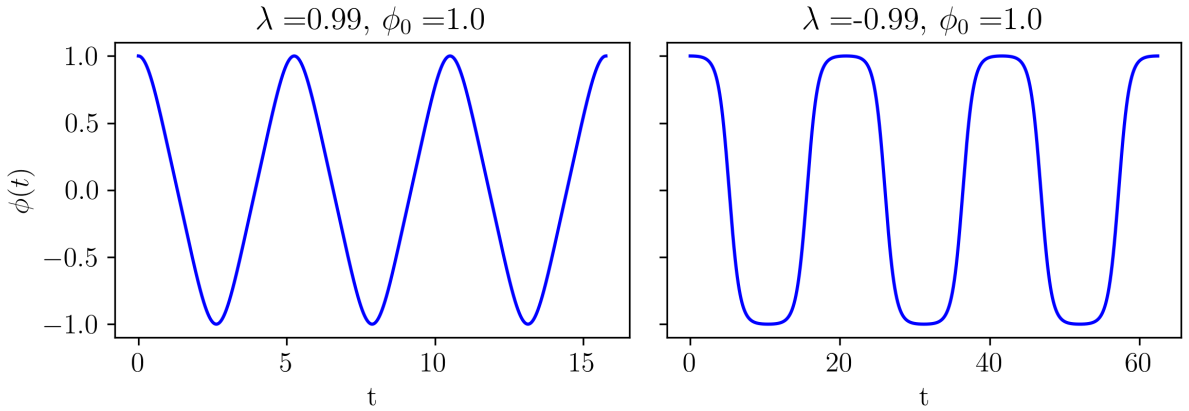


Figure 3.3: These are extreme cases of  $\lambda$  and  $\phi_0$  values. At small  $\lambda$  and  $\phi_0$ , the motion resembles a simple cosine.

Define

$$\omega = \sqrt{m^2 + \lambda\phi_0^2}, \quad m = \sqrt{\frac{\lambda\phi_0^2}{2(m^2 + \lambda\phi_0^2)}} \quad (3.11)$$

and

$$\bar{\omega} = \sqrt{m^2 + \frac{\lambda\phi_0^2}{2}}, \quad \bar{m} = \sqrt{-\frac{\lambda\phi_0^2}{2m^2 + \lambda\phi_0^2}} \quad (3.12)$$

which are chosen<sup>12</sup> such that  $\phi(t) = \phi_0 \operatorname{cn}(\omega t, m)$  for  $\lambda > 0$ , and  $\phi(t) = \phi_0 \operatorname{cd}(\bar{\omega}t, \bar{m})$  for  $\lambda < 0$ . The Jacobi elliptic functions have periods of oscillation which can be found explicitly

$$T = \begin{cases} 4K(m)/\omega & \text{if } \lambda > 0 \\ 4K(\bar{m})/\bar{\omega} & \text{if } \lambda < 0 \end{cases} \quad (3.13)$$

where  $K(\cdot)$  is the Jacobi complete elliptic integral of the first kind.

### 3.3.2 Integrate for Inflaton Perturbations

Using equations 3.9, 3.10 and 3.13, we can solve for the inflaton perturbations after one period with reduced numerical error as  $\phi(t)$  and  $T$  are given explicitly. We solve the system of equations for  $j = 1, 2$ ,

$$\begin{pmatrix} \delta\dot{\phi}_k^{(j)} \\ \delta\ddot{\phi}_k^{(j)} \end{pmatrix} = \begin{pmatrix} 0 & 1 \\ -[k^2 + m^2 + 3\lambda\phi_0^2 \operatorname{cn}(\omega t, m)^2] & 0 \end{pmatrix} \begin{pmatrix} \delta\phi_k^{(j)} \\ \delta\dot{\phi}_k^{(j)} \end{pmatrix} \text{ if } \lambda > 0 \quad (3.14)$$

$$\begin{pmatrix} \delta\dot{\phi}_k^{(j)} \\ \delta\ddot{\phi}_k^{(j)} \end{pmatrix} = \begin{pmatrix} 0 & 1 \\ -[k^2 + m^2 + 3\lambda\phi_0^2 \operatorname{cd}(\bar{\omega}t, \bar{m})^2] & 0 \end{pmatrix} \begin{pmatrix} \delta\phi_k^{(j)} \\ \delta\dot{\phi}_k^{(j)} \end{pmatrix} \text{ if } \lambda < 0 \quad (3.15)$$

for different  $k$  and  $\phi_0$  and use Floquet theory to find its stability.

### 3.3.3 Mathieu Stability Charts

Alternatively, we can approximate the Jacobi cosine function as a regular cosine function for  $\lambda > 0$  — the resulting differential equation for  $\delta\phi_k$  will be of the form

$$\frac{d^2\delta\phi_k}{d\tau^2} + [a - 2b \cos(2\tau)]\delta\phi_k(\tau) = 0 \quad (3.16)$$

where  $a$  and  $b$  are free parameters, and  $\tau = \nu t$  for some  $\nu$ . This is called the Mathieu equation, of which there exists an explicit equation for its Floquet exponents for arbitrary  $a$  and  $b$  [11] (see figure 3.4). Hence, we bypass the need for any numerical integration.

There always exists a solution to the Mathieu equation of the form<sup>3</sup>

$$\delta\phi(\tau) = \mathcal{P}(\tau)e^{i\mu\tau} + \mathcal{P}(-\tau)e^{-i\mu\tau} \quad (3.17)$$

where  $\mathcal{P}(\tau)$  is a  $\pi$ -periodic function and  $\mu \in \mathbb{C}$ . Then

$$\mu = \frac{2}{\pi} \sin^{-1} \left( \sqrt{\Delta(0) \sin^2 \left( \frac{\pi}{2} \sqrt{a} \right)} \right) \quad (3.18)$$

---

<sup>1</sup>This ‘frequency’ term isn’t the actual frequency of oscillations of  $\phi(t)$ ;  $\omega, \bar{\omega} \neq 2\pi/\text{Period}$ .

<sup>2</sup>Careful that the modulus  $m$  is un-italicised and mass quantity  $m$  is italicised.

<sup>3</sup>Notice the multiplication by  $i$  compared to the lack thereof in equation 3.1.

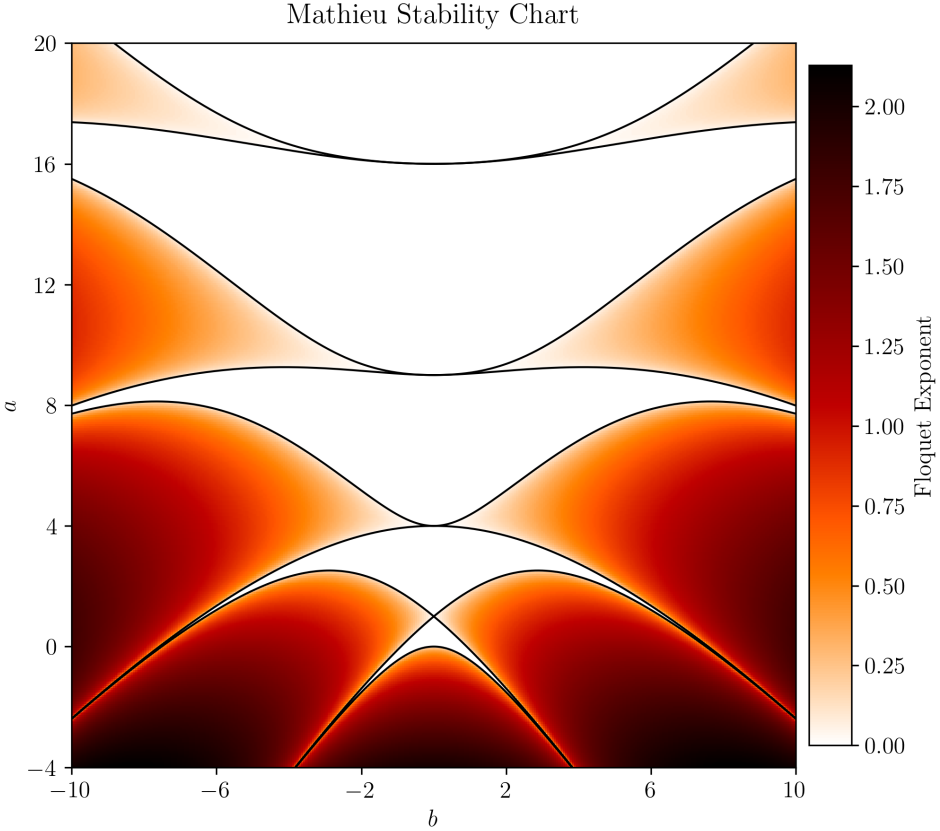


Figure 3.4: The white lines are the even and odd characteristic values for the Mathieu equations. The regions of the  $a$ - $b$  parameter space which are black and in between the characteristic values represent Floquet exponents which are identically 0; everywhere else in the parameter space represents varying degrees of instability of solutions to the Mathieu equation.

where  $\Delta(\mu)$  is the determinant of an infinite dimensional tridiagonal matrix

$$\Delta(\mu) = \det \begin{pmatrix} \ddots & \dots & \dots & \dots & \dots & \dots & \ddots \\ \vdots & 1 & \frac{b}{(\mu-4)^2-a} & 0 & 0 & 0 & \vdots \\ \vdots & \frac{b}{(\mu-2)^2-a} & 1 & \frac{b}{(\mu-2)^2-a} & 0 & 0 & \vdots \\ \vdots & 0 & \frac{b}{\mu^2-a} & 1 & \frac{b}{\mu^2-a} & 0 & \vdots \\ \vdots & 0 & 0 & \frac{b}{(\mu+2)^2-a} & 1 & \frac{b}{(\mu+2)^2-a} & \vdots \\ \vdots & 0 & 0 & 0 & \frac{b}{(\mu+4)^2-a} & 1 & \vdots \\ \ddots & \dots & \dots & \dots & \dots & \dots & \ddots \end{pmatrix}. \quad (3.19)$$

In practice, we just need to compute the determinant of a large matrix centered around  $\begin{pmatrix} \ddots & \frac{b}{(\mu-2)^2-a} & 0 \\ \frac{b}{\mu^2-a} & 1 & \frac{b}{\mu^2-a} \\ 0 & \frac{b}{(\mu+2)^2-a} & \ddots \end{pmatrix}$ ; for my graphs, I chose a  $101 \times 101$  matrix. The Floquet exponent expressed in terms of the unscaled time  $t$  is  $\Re(\mu_k) = \frac{\Im(\mu)}{\nu}$ .

### Solutions for $\lambda > 0$

The Jacobi  $\text{cn}(\omega t, m)$  function can be written as a linear combination of cosines. First, define the nome and frequency, respectively denoted  $q$  and  $\nu$

$$q = \exp\left(-\frac{\pi K(1-m)}{K(m)}\right) \text{ and } \nu = \frac{\pi\omega}{2K(m)} \quad (3.20)$$

hence

$$\text{cn}(\omega t, m) = \frac{2\pi}{\sqrt{m}K(m)} \sum_{n=0}^{\infty} \frac{q^{n+1/2}}{1+q^{2n+1}} \cos((2n+1)\nu t) \quad (3.21)$$

and taking only the first order term,

$$\text{cn}(\omega t, m) \approx \frac{2\pi}{\sqrt{m}K(m)} \frac{\sqrt{q}}{1+q} \cos(\nu t). \quad (3.22)$$

This yields the differential equation for  $\delta\phi_k$

$$\ddot{\delta\phi}_k + \left[ k^2 + m^2 + \frac{6\pi^2\lambda\phi_0^2}{mK(m)^2} \frac{q}{(1+q)^2} + \frac{6\pi^2\lambda\phi_0^2}{mK(m)^2} \frac{q}{(1+q)^2} \cos(2\nu t) \right] \delta\phi_k = 0 \quad (3.23)$$

using the trigonometric identity  $2\cos(\theta)^2 = 1 + \cos(2\theta)$ . Applying the transformation  $\tau = \nu t$  yields the final DE

$$\frac{d^2\delta\phi_k}{d\tau^2} + \left[ \frac{1}{\nu^2} \left( k^2 + m^2 + \frac{6\pi^2\lambda\phi_0^2}{mK(m)^2} \frac{q}{(1+q)^2} \right) + \frac{\lambda\phi_0^2}{\nu^2} \frac{6\pi^2}{mK(m)^2} \frac{q}{(1+q)^2} \cos(2\tau) \right] \delta\phi_k = 0. \quad (3.24)$$

with parameters  $a$  and  $b$  defined appropriately to match the form of equation 3.16. We can hence solve for its Floquet exponents using equations 3.18 and 3.19.

### Solutions for $\lambda < 0$

The Jacobi  $\text{cd}(\bar{\omega}t, \bar{m})$  function can also be written as a ratio of infinite series of cosines. Define the nome and frequency respectively  $\bar{q}$  and  $\bar{\nu}$

$$\bar{q} = \exp\left(-\frac{\pi K(1-\bar{m})}{K(\bar{m})}\right) \text{ and } \bar{\nu} = \frac{\pi\bar{\omega}}{2K(\bar{m})} \quad (3.25)$$

hence

$$\text{cd}(\bar{\omega}t, \bar{m}) = \frac{\text{cn}(\bar{\omega}t, \bar{m})}{\text{dn}(\bar{\omega}t, \bar{m})} = \frac{\frac{2\pi}{\sqrt{\bar{m}}K(\bar{m})} \sum_{n=0}^{\infty} \frac{q^{n+1/2}}{1+q^{2n+1}} \cos((2n+1)\nu t)}{\frac{2\pi}{K(\bar{m})} + \frac{2\pi}{K(\bar{m})} \sum_{n=1}^{\infty} \frac{\bar{q}^n}{1+\bar{q}^{2n}} \cos(2n\bar{\nu}t)} \quad (3.26)$$

where  $\text{dn}(\cdot, \cdot)$  is another Jacobi elliptic function. Assuming that  $\text{cd}(\bar{\omega}t, \bar{m})$  are close to sinusoidal, i.e.  $\bar{m} \rightarrow 0$  and hence  $\bar{q} \rightarrow 0$ ,  $\bar{q}$  and its higher order terms negligible compared to  $\sqrt{\bar{q}}$ ;

$$\text{cd}(\bar{\omega}t, \bar{m}) \approx \frac{4\sqrt{\bar{q}}}{\sqrt{\bar{m}}} \cos(\bar{\nu}t). \quad (3.27)$$

Applying the transformation  $\tau = \bar{\nu}t$ , the DE for  $\delta\phi_k$  for  $\lambda < 0$  becomes

$$\frac{d^2\delta\phi_k}{d\tau^2} + \left[ \frac{1}{\bar{\nu}^2} \left( k^2 + m^2 + \lambda\phi_0^2 \frac{24\bar{q}}{\bar{m}} \right) + \frac{\lambda\phi_0^2}{\bar{\nu}^2} \frac{24\bar{q}}{\bar{m}} \cos(2\tau) \right] \delta\phi_k = 0 \quad (3.28)$$

which also resembles equation 3.16 if  $a$  and  $b$  are defined appropriately and can likewise have its Floquet exponents solved.

We will return to these solutions in the following chapter.

# Chapter 4

## The Monodromy Potential

In this chapter, I examine the resonance structure of the Monodromy model; in particular, the limits wherein it overlaps with the  $V_4(\phi)$  and  $V_6(\phi)$  potential. Additionally, with regard to the quartic potential, I investigate the efficacy of approximating the inflaton perturbations as solutions to the Mathieu equation. All stability charts shown have bands of non-zero Floquet exponents representing values in the  $k\text{-}\phi_0$  parameter space which exhibit unstable growth of the inflaton perturbations — these are called resonance bands.

### 4.1 Summary of the Monodromy Potential

I split my analysis of the Monodromy model into  $\alpha < 1$  and  $\alpha > 1$ . Figure 4.1 shows sample stability charts generated from the Monodromy potential through integrating equation 3.5, one representative of  $\alpha < 1$  models and the other representative of  $\alpha > 1$  models.

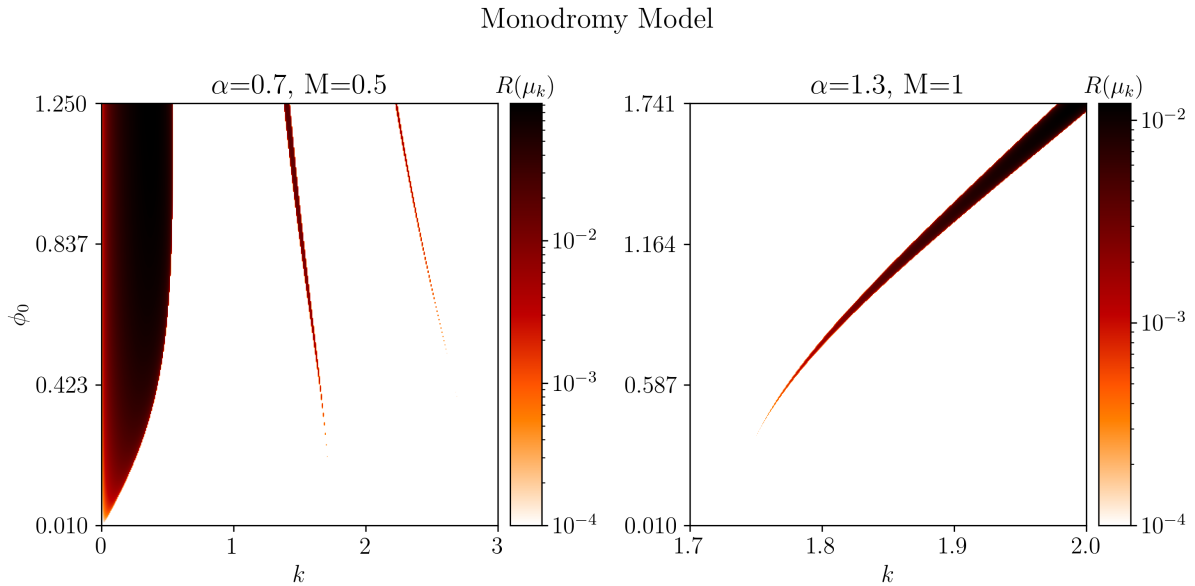


Figure 4.1: Stability charts generated from the Monodromy model with  $\alpha = 0.5, M = 0.5$  and  $\alpha = 1.3, M = 1$  respectively.

The greatest qualitative difference is the existence of a large resonance band hugging the  $k = 0$  axis for  $\alpha < 1$  and the lack thereof for  $\alpha > 1$ . As the universe expands, inflaton perturbations will spend most of their time in the low  $k\text{-}\phi_0$  region, hence the existence of the low  $k$  resonance band for  $\alpha < 1$  Monodromy potentials will contribute significantly to the growth of inflaton perturbations during preheating;  $\alpha > 1$  will be unproductive in this regard. For both  $\alpha < 1$  and

$\alpha > 1$ , away from  $k = 0$ , there are thin resonance bands present in both models which become weaker for higher  $k$  which will contribute minimally to the growth of perturbations. The value of  $\alpha$  has little effect on the shape of resonance bands, but weakens the strength of the regions of resonance as  $\alpha$  approaches 1. The value of  $M$  affects the shape of the bands more, where smaller values of  $M$  generally lead to thicker resonance bands with higher Floquet exponent, and vice versa.

## 4.2 The Quartic and Sixth Order Terms

We compare the stability charts generated with the Monodromy model with parameters  $\alpha \in \{0.7, 0.9, 0.95, 1.05, 1.1, 1.3\}$  and  $M \in \{0.5, 1, 2\}$  with the corresponding charts generated with the  $V_4(\phi)$  and  $V_6(\phi)$  potentials, where  $\lambda$  and  $g$  are determined according to equation 2.21. This range of  $\alpha$  and  $M$  are chosen as these lead to the best agreement between the Monodromy potential and the forth and sixth order Taylor expansions. In the interest of brevity, below I have only shown the comparisons for  $\alpha = 0.7$  and  $1.3$  for all  $M$  (figures 4.2 and 4.3) which are sufficient in displaying relevant features; the rest of the comparisons are in Appendix A. Note that all stability bands shown in these stability charts (and those in Appendix A) are continuous — the broken bands are a limitation of the finite resolution which these images are produced with. Nevertheless, the broken bands highlight how thin some of the stability bands are.

For  $\alpha = 1.3$  (and all  $\alpha \gtrsim 1$ ) (see figure 4.2), there are no resonance bands hugging the  $k = 0$  axis for most of the stability charts; there are only sparsely distributed thin resonance bands which becomes weaker as  $k$  increases, of which I have plotted only the first dominant resonance band. There is general agreement between the Monodromy and quartic stability charts, however the shape, range of these stability bands don't match. Regarding the agreement of the  $V_6(\phi)$  potential, there is great agreement for  $M = 2$ , better than the corresponding quartic potential; however this agreement quickly breaks down for smaller  $M$  with the stability band becoming thicker and stronger, and the appearance of a  $k = 0$  hugging resonance band for  $M = 0.5$ . For  $\alpha = 0.7$  (and all  $\alpha \lesssim 1$ ) (see figure 4.3), it is apparent that almost all Monodromy models will need more than the fourth and sixth order terms to reproduce its stability charts. The stability charts produced by the  $V_4(\phi)$  potential for all  $M$  do not reproduce those of the Monodromy model, particularly regarding the shape of the  $k = 0$  axis hugging stability band; more about this band will be covered later in this chapter. Subsequent stability bands resemble those of the Monodromy model better, but are still about an order of magnitude weaker and span a different range of  $k$ . Regarding the  $V_6(\phi)$  potential, the stability chart produced by  $M = 2$  resembles that of the Monodromy model well, in which case not many more Taylor expansion terms would be needed to achieve better resemblance. As  $M$  decreases, the qualities of the  $\phi^6$  potential stability charts depart greatly from the corresponding charts produced by the full Monodromy potential.

For all values of  $\alpha < 1$ ,  $\alpha > 1$  and  $M$ , the quartic potential is nowhere sufficient to reproduce the resonant structure of the Monodromy model. The quartic potential does not contain enough information resemble the finer aspects of the Monodromy potential about its minima. For all  $\alpha < 1$  and  $\alpha > 1$ , the degree which the stability charts generated by the  $V_6(\phi)$  potential overlap with those generated by the Monodromy potential is highly dependent on the value of  $M$ . Particularly, Monodromy and  $V_6(\phi)$  charts produced with smaller  $M$  completely disagree for higher  $\phi_0$ . This is not necessarily surprising as values of the coefficients of the forth and sixth order terms,  $\lambda$  and  $g$ , scale like  $1/M^2$  and  $1/M^4$  respectively, meaning the Monodromy potential is approximated worse for lower  $M$ . In fact, the  $V_4(\phi)$  potential reproduces the resonant structures of the Monodromy model better than the  $V_6(\phi)$  potential; the sixth order term dominates too much of the shape of the potential for smaller  $M$ , leading to greater disagreement. Charts

produced with larger  $M$  are almost identical, and may not need higher order terms to reproduce the structures of the Monodromy model.

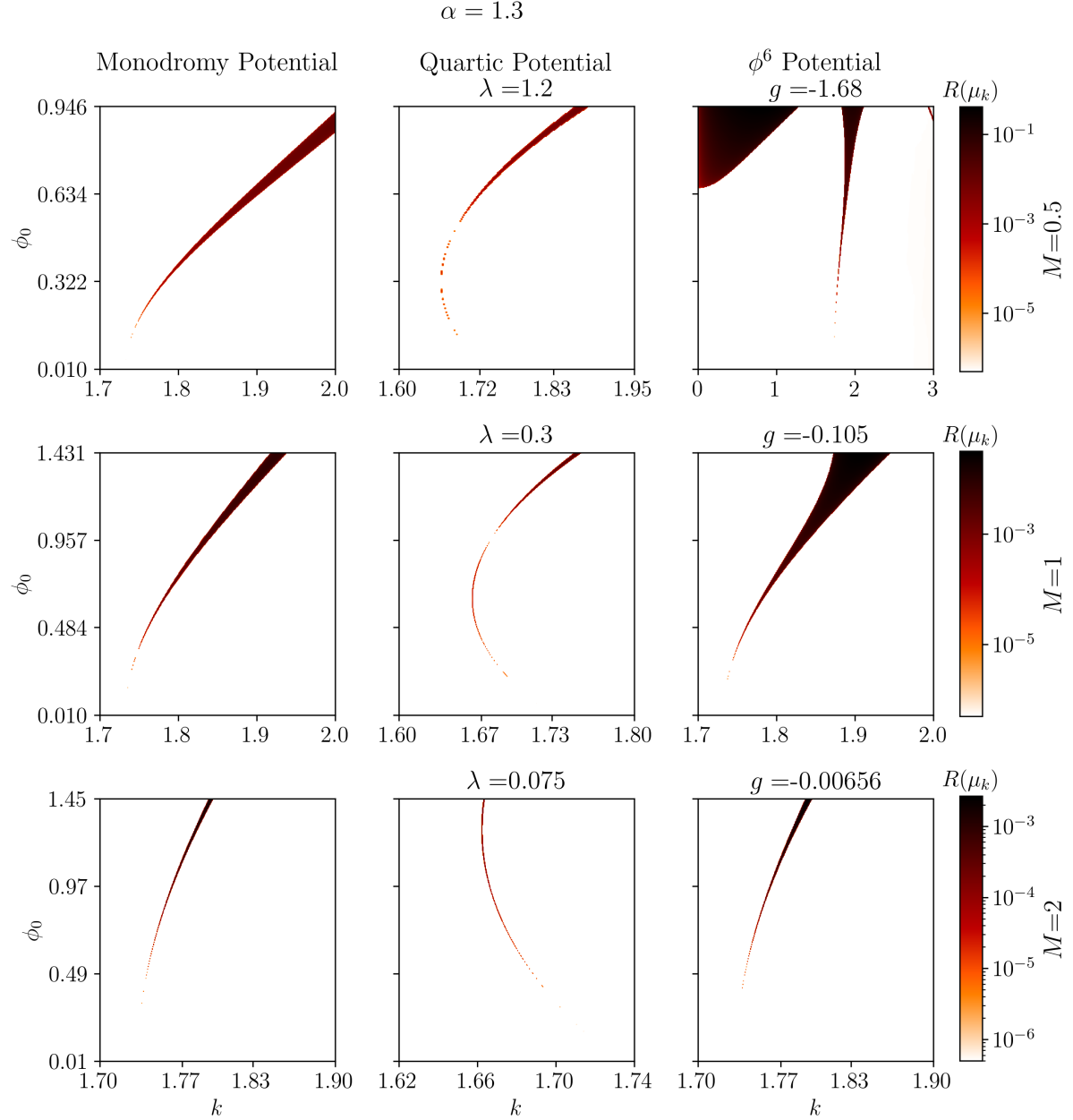


Figure 4.2: Comparing the three potentials with  $\alpha = 1.3$  and varying  $M \in \{0.5, 1, 2\}$ , zoomed about first dominant resonance band.

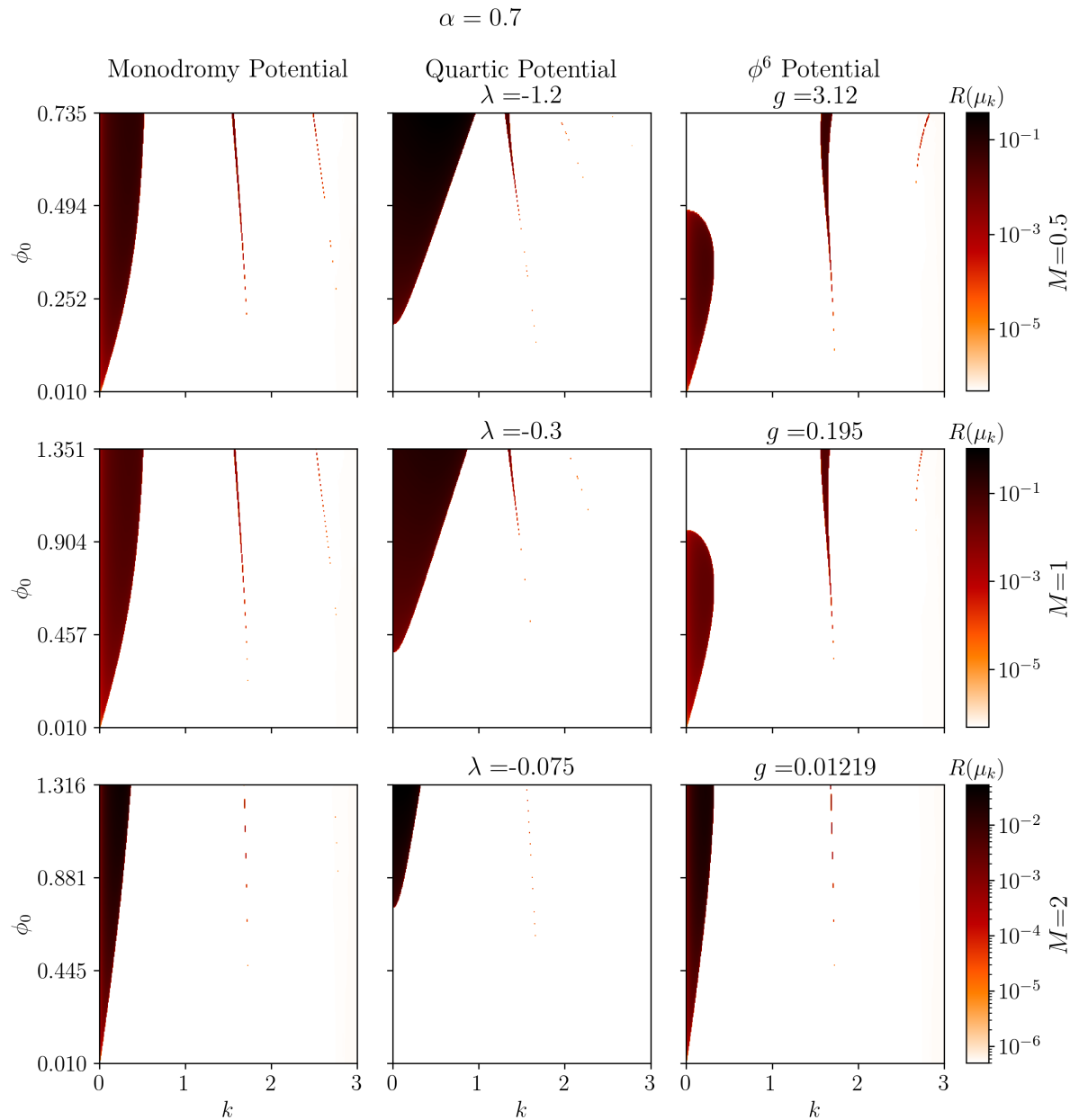


Figure 4.3: Comparing the three potentials with  $\alpha = 0.7$  and varying  $M \in \{0.5, 1, 2\}$ .

### 4.3 Results from Mathieu Equation

Regarding the quartic potential, I compared the stability charts generated from approximating inflaton perturbations as solutions to the Mathieu equation against those generated from integrating equation 3.14. I plotted charts for  $\lambda \in \{-0.2, -0.005, 0.005, 0.2\}$  for both cases (figure 4.4). Points in the stability charts produced with the Mathieu equation which appear to be 0 are identically 0.

All stability bands are almost identical in shape and position in the  $k$ - $\phi_0$  plane, differing slightly in thickness and strength. For smaller values of  $|\lambda|$ , the strength and thickness of the stability bands are underestimated; for larger values of  $|\lambda|$ , the strength and thickness of the stability bands are overestimated. Qualitatively and analytically, this approximation is very accurate and fairly precise. Regarding the resonant band hugging the  $k = 0$  axis in produced by the quartic potential for  $\lambda < 0$ , see middle columns of figures 4.3, A.1, A.2, it appears that this band does not reach to  $\phi_0 = 0$ . Furthermore, this band climbs up the  $\phi_0$  axis as  $\lambda$  approaches 0 before disappearing from the  $k$ - $\phi_0$  space of interest. This is confirmed by the the usage of the Mathieu equations; this is explained next.

We may get a better understanding of where the resonance bands lie on the  $k$ - $\phi_0$  plane by looking at where the  $k$ - $\phi_0$  space lies on the original Mathieu stability chart, see figure 4.5 and 4.6. The explicit relationship for  $a$  and  $b$  of the Mathieu equation with respect to  $\lambda, \phi_0$  and  $k$  is

$$a = \begin{cases} \frac{1}{\nu^2} \left( k^2 + m^2 + \frac{6\pi^2 \lambda \phi_0^2}{m K(m)^2} \frac{q}{(1+q)^2} \right) & \lambda > 0 \\ \frac{1}{\bar{\nu}^2} \left( k^2 + m^2 + \lambda \phi_0^2 \frac{24\bar{q}}{\bar{m}} \right) & \lambda < 0 \end{cases} \quad (4.1)$$

$$b = \begin{cases} -\frac{\lambda \phi_0^2}{\nu^2} \frac{3\pi^2}{m K(m)^2} \frac{q}{(1+q)^2} & \lambda > 0 \\ -\frac{\lambda \phi_0^2}{\bar{\nu}^2} \frac{12\bar{q}}{\bar{m}} & \lambda < 0 \end{cases} \quad (4.2)$$

The value of  $b$  (on the horizontal axis) depends only on the value of  $\lambda \phi_0^2$ . The value of  $a$  (on the vertical axis) depends on  $\lambda \phi_0^2$  and strictly increases with  $k$ . To find where values of  $k$ - $\phi_0$  of interest lie on the  $a$ - $b$  parameter space, I mapped out the values of  $a$  and  $b$  evaluated at  $\phi_{\text{end}}$  for some  $-0.2 \leq \lambda \leq 0.2$ , and  $k$  ranging from 0 to a large number. The minimum value of  $a$  occurs at  $k = 0$  for all  $\lambda \phi_0^2$ . In figure 4.5 about the  $b = 0$  axis, there exists regions of instability near all values of square values of  $a$ . These regions will hence map to an infinite number of resonance bands the  $k$ - $\phi_0$  space at different values of  $k$ , becoming more sparse and weaker for increasing  $k$ . The values of  $\lambda > 0$  corresponds to the  $b < 0$  side of the Mathieu stability chart. we can see in figure 4.5 and 4.6 that for all small  $\lambda < 0$ , the line of the  $k$ - $\phi_0$  space which corresponds to  $k = 0$  (bottom of the blue shapes in the figures) never cross a region of instability in the  $a$ - $b$  space; hence there will never be a resonance band hugging the  $k = 0$  axis of the stability charts. The values of  $\lambda < 0$  corresponds to  $b > 0$ ; by a similar argument, only some values of  $\lambda$  will have a resonance band which hugs the  $k = 0$  axis. Referring to figure 4.6, smaller values of  $\lambda < 0$  correspond to smaller values of  $b > 0$ . If  $\lambda$  is sufficiently small, then there will be no resonance band hugging the  $k = 0$  axis and vice versa if  $\lambda$  is sufficiently large. This matches the stability charts shown.

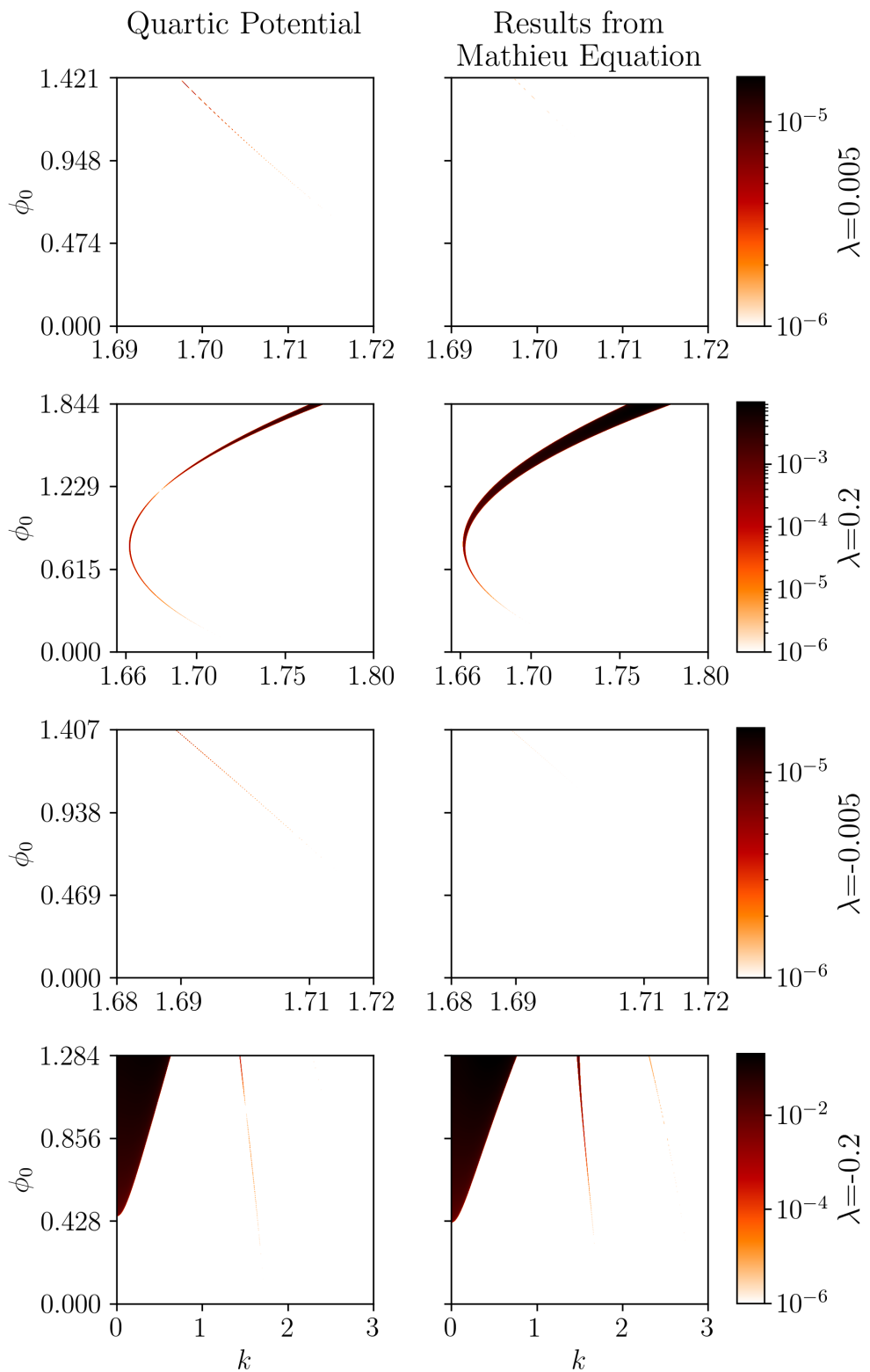


Figure 4.4: Stability charts generated by integrating equation 3.14 (left column) and those generated by approximating perturbations as solutions to the Mathieu equation (right column). The bands on the first and third figure of the right column are very fine and faint; otherwise their shape and position is identical to those on the left column.

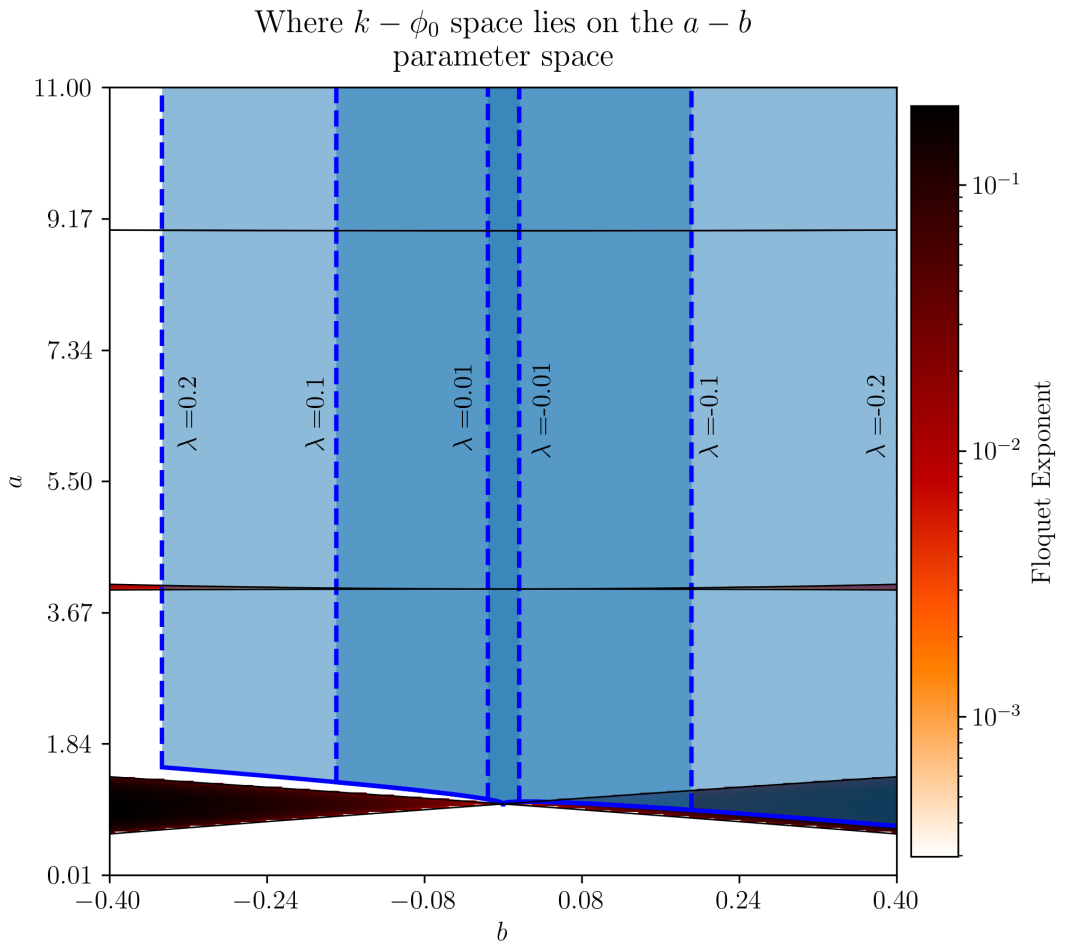


Figure 4.5: The Mathieu stability chart zoomed about the  $b = 0$  axis. Most values of  $a$  and  $b$  result in stable perturbations. Spaces which signify non-stable perturbations are enclosed by the characteristic values of even and odd Mathieu equations. The blue spaces map the  $k - \phi_0$  space of interest to the  $a - b$  parameter space, where the bottom of these shapes map to  $k = 0$  values. The vertical dashed lines are values of  $b$  evaluated at  $\lambda\phi_{\text{end}}^2$ .

Where  $k - \phi_0$  space lies on the  $a - b$   
parameter space; zoomed about  $a = 1, b = 0$

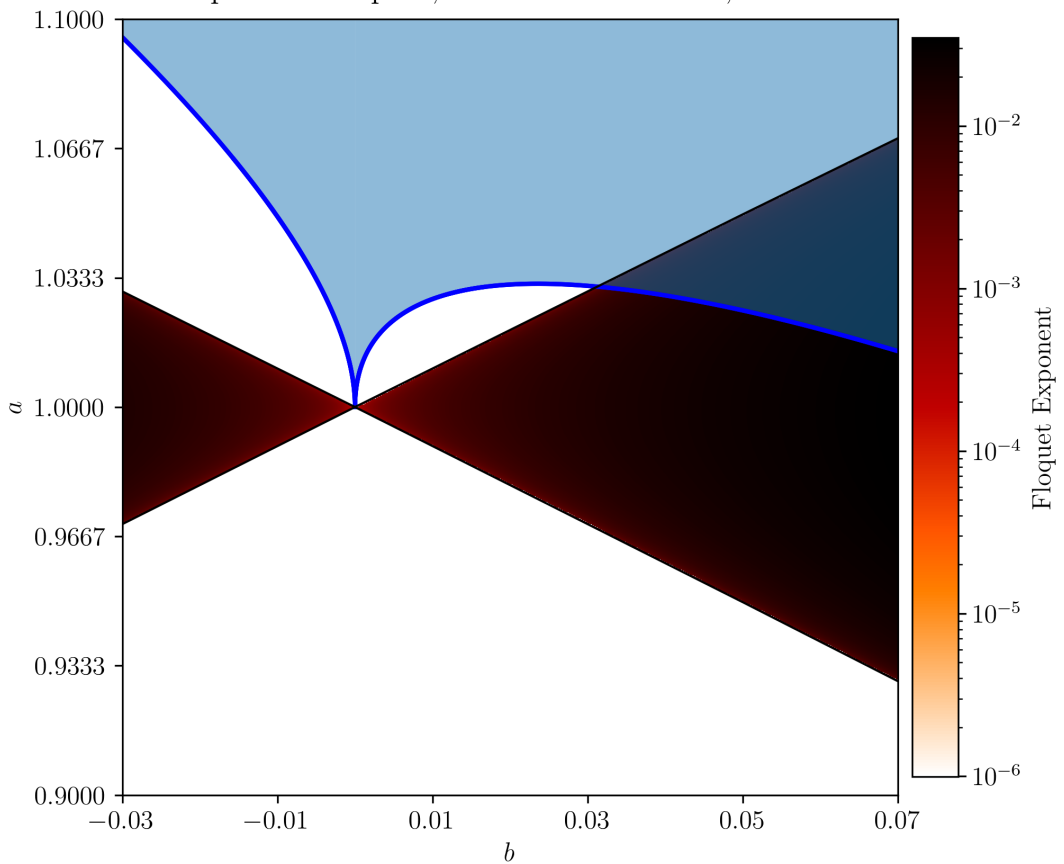


Figure 4.6: Same as figure 4.5 but zoomed in about  $a = 1, b = 0$ .

## 4.4 Accuracy of Results

### 4.4.1 Accuracy of the Differential Equation as a Mathieu Equation

We investigate the accuracy of approximating the inflaton perturbations as solutions to the Mathieu equations. For  $\lambda > 0$ , compare  $\text{cn}(\omega t, m)$  to its cosine approximation according to equation 3.22;

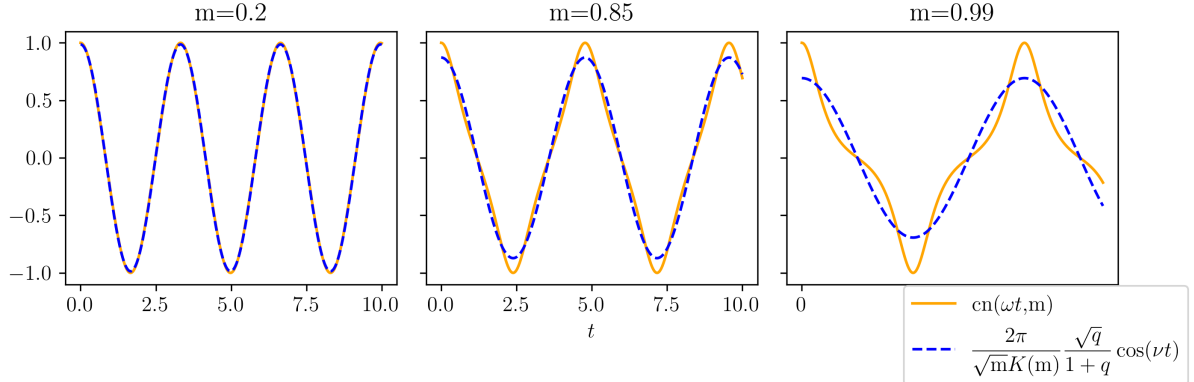


Figure 4.7:  $\text{cn}(\omega t, m)$  and its first order cosine approximation for various moduli  $m$ .

The frequency of the cosine approximation  $\nu$  is always exactly the frequency of the Jacobi cosine function as per its definition<sup>1</sup>. Hence, the only contributing parameter to the accuracy of the approximation is the modulus  $m$  which controls the shape of the Jacobi cosine function and hence how well it can be approximated by a single cosine term. In principle,  $m$  is bounded between 0 and 1. As  $m \rightarrow 0$ ,  $\text{cn}(\omega t, m) \rightarrow \frac{2\pi}{\sqrt{m}K(m)} \frac{\sqrt{q}}{1+q} \cos(\nu t)$ , i.e. approximating  $\text{cn}(\omega t, m)$  as a cosine is more accurate for smaller  $m$ . Recall the definition of  $m$  in equation 3.11 which is monotonically increasing with  $\lambda\phi_0^2$  and asymptotes to  $1/\sqrt{2} \approx 0.707$ . Additionally, the amplitude of background oscillations  $\phi_0$  has a maximum value at the end of inflation  $\phi_{\text{end}}$  from which it decreases as the universe expands.  $\phi_{\text{end}}$  monotonically increases with  $\lambda$  — this sets an upper bound on the value of  $\lambda\phi_0^2$  for each  $\lambda$  and hence a different upper bound on the modulus  $m$ .

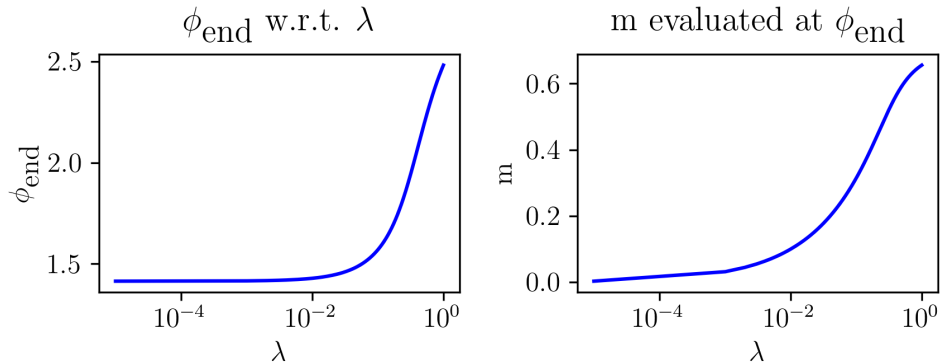


Figure 4.8:  $\phi_{\text{end}}$  and  $\max\{m\}$  with respect to  $\lambda$ . Both of these asymptote at values of  $\lambda$  too large for us to consider.

We may quantify how accurate the first order approximation is of the Jacobi cosine function by looking at the contributions from all higher order terms. Consider the series of the coefficient

<sup>1</sup> $\nu \equiv \frac{\pi\omega}{2K(m)} = \frac{2\pi}{T}$  where  $T$  is the period of the the Jacobi elliptic functions as stated in equation 3.13.

terms of the expansion of equation 3.21

$$\sum_{n=0}^{\infty} \frac{2\pi}{\sqrt{m}K(m)} \frac{q^{n+1/2}}{1+q^{2n+1}} \quad (4.3)$$

which is equivalent to the series equation 3.21 evaluated at  $t = 0$ . All terms in this series are positive, meaning the partial series is strictly increasing. Additionally, at  $t = 0$ , the Jacobi cosine function evaluates to 1 for all  $m$ , meaning this infinite series must also evaluate to 1. Hence if the first order expansion term is sufficiently close to 1, we can consider the contributions from each higher order term as being negligible. For all  $\lambda$ , I evaluated  $m$  at  $\phi_{\text{end}}$ . We find that that minimum contribution from only the first term of the expansion is greater as  $\lambda$  decreases.

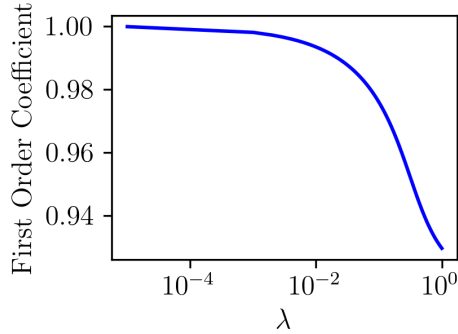


Figure 4.9: For all  $\lambda$ , I evaluated the coefficient of the first order term at  $\phi_{\text{end}}$ . All other  $\phi_0 < \phi_{\text{end}}$  for all  $\lambda$  will have a higher contribution from the first term. At  $\lambda = 0.2$  and  $\phi_{\text{end}}$ , the first order coefficient is 0.963.

For  $\lambda < 0$ , compare  $\text{cd}(\bar{\omega}t, \bar{m})$  to its cosine approximation according to equation 3.27;

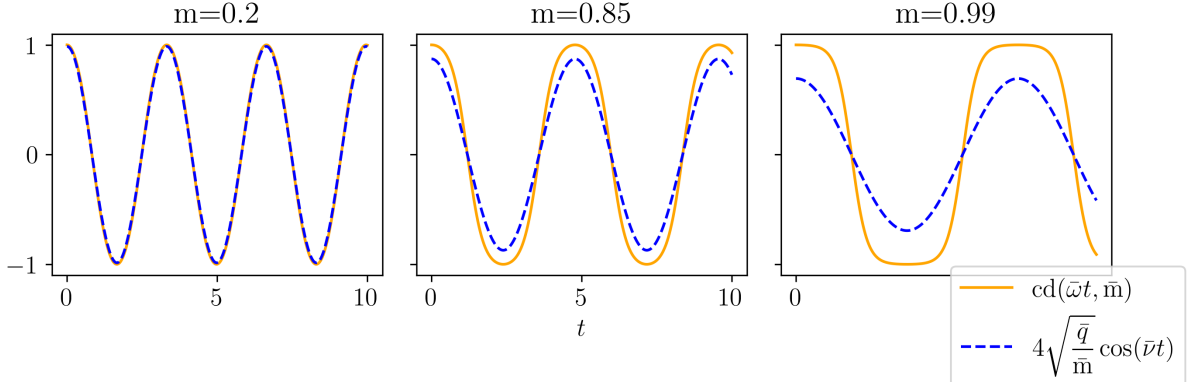


Figure 4.10:  $\text{cd}(\bar{\omega}t, \bar{m})$  and its first order cosine approximation for various modulus  $\bar{m}$ .

Similarly to the  $\lambda > 0$  cases, the frequency of the cosine approximation is exactly the same as the frequency of the Jacobi  $\text{cd}(\cdot, \cdot)$  function as per its definition — hence we need only to look at how the modulus  $\bar{m}$  affects the accuracy of the approximation. Again, as  $\bar{m} \rightarrow 0$ ,  $\text{cd}(\bar{\omega}t, \bar{m}) \rightarrow 4\sqrt{\frac{\bar{q}}{\bar{m}}} \cos(\bar{\nu}t)$  where now  $\bar{m}$  is bounded between 0 and 1 for  $-m^2 < \lambda\phi_0^2 < 0$  and  $\bar{m}$  monotonically increases with  $|\lambda\phi_0^2|$ . The maximum value of  $|\lambda\phi_0^2|$  we need to consider for each  $\lambda$  occurs at  $\phi_{\text{end}}$  which increases monotonically with  $\lambda$ , hence the upper bound of  $\bar{m}$  decreases monotonically with  $\lambda$  as shown in figure 4.11.

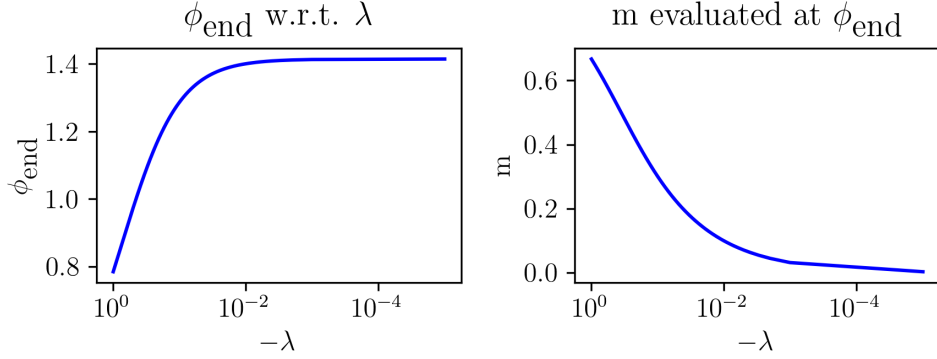


Figure 4.11:  $\phi_{\text{end}}$  and  $\max\{m\}$  with respect to a reasonable range of  $-\lambda$ .

To quantitatively assess the accuracy of the approximation of equation 3.27, we need to consider the affects of assuming  $\bar{m} \rightarrow 0 \implies \bar{q} \rightarrow 0 \implies \sqrt{\bar{q}} \ll \text{higher order terms}$ . First, consider the affects on the approximation of the Jacobi  $\text{cn}(\cdot, \cdot)$  function;

$$\text{cn}(\bar{\omega}t, \bar{m}) = \frac{2\pi}{\sqrt{m}K(m)} \sum_{n=0}^{\infty} \frac{\bar{q}^{n+1/2}}{1 + q^{2n+1}} \cos((2n+1)\bar{\nu}t) \approx \frac{2\pi\sqrt{\bar{q}}}{\sqrt{m}K(m)} \cos(\bar{\nu}t). \quad (4.4)$$

Since the amplitude of  $\text{cn}(\cdot, \cdot)$  is 1 and all terms with higher order values of  $\bar{q}$  are strictly positive, we know that the contributions from the the terms with higher order  $\bar{q}$  are negligible if  $\frac{2\pi\sqrt{\bar{q}}}{\sqrt{m}K(m)}$  is close to 1, see figure 4.12. Consider the affects of assuming small  $\bar{q}$  on the approximation of the  $\text{dn}(\cdot, \cdot)$  function;

$$\text{dn}(\bar{\omega}t, \bar{m}) = \frac{\pi}{2K(m)} + \frac{2\pi}{K(m)} \sum_{n=1}^{\infty} \frac{\bar{q}^n}{1 + q^{2n}} \cos(2n\bar{\nu}t) \approx \frac{\pi}{2K(m)}, \quad (4.5)$$

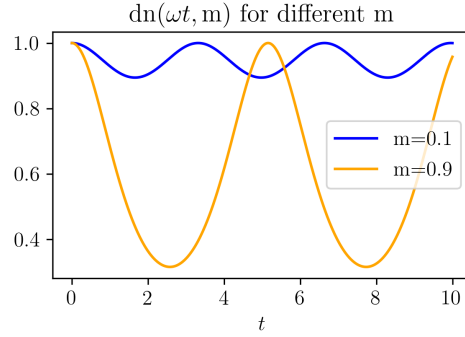


Figure 4.12: Caption

The  $\text{dn}(\cdot, \cdot)$  function oscillates about  $\frac{\pi}{2K(m)} > 0$  and always has a maximum value of 1, hence the amplitude of the oscillations is  $\frac{1}{2} \left( 1 - \frac{\pi}{2K(m)} \right)$ . If  $\frac{\pi}{2K(m)}$  is sufficiently close to 1, then the contributions from the oscillations of  $\text{dn}(\cdot, \cdot)$  is negligible.

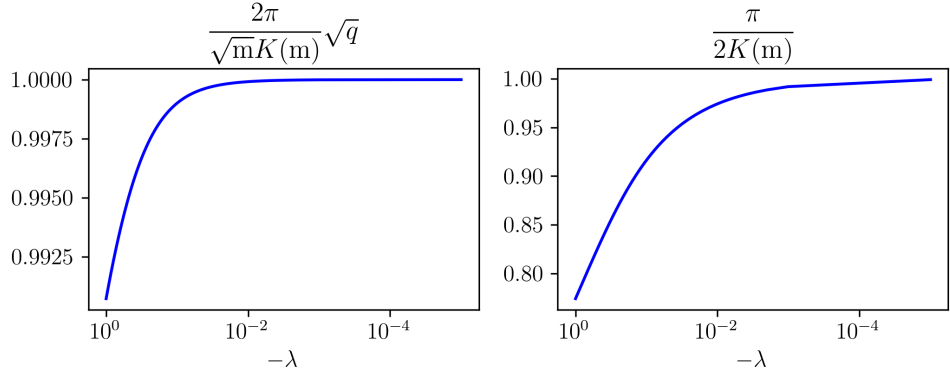


Figure 4.13: The left figure shows the size of the amplitude of the  $\text{cn}(\cdot, \cdot)$  function when approximated with small  $\bar{q}$  and the right figure shows the constant term of the  $\text{dn}(\cdot, \cdot)$ , both with respect to  $\lambda$  and calculated at  $\phi_{\text{end}}$  at each  $\lambda$ . At  $\lambda = -0.2$ , the amplitude of oscillations of  $\text{cn}(\cdot, \cdot)$  approximated as a cosine function is 0.998, and the constant term of the  $\text{dn}(\cdot, \cdot)$  function is 0.882.

#### Accuracy of obtaining the correct Mathieu stability chart

Although there exists an analytic solution to the Mathieu stability chart, the equation used equation 3.18 required the determinant of an infinite dimensional matrix equation 3.19. Hence, in order to solve for the Floquet exponents accurately using a finite square matrix, it appears a bigger matrix is superior, demonstrated in figure 4.14. I calculated the determinant of a  $101 \times 101$  matrix for my results.

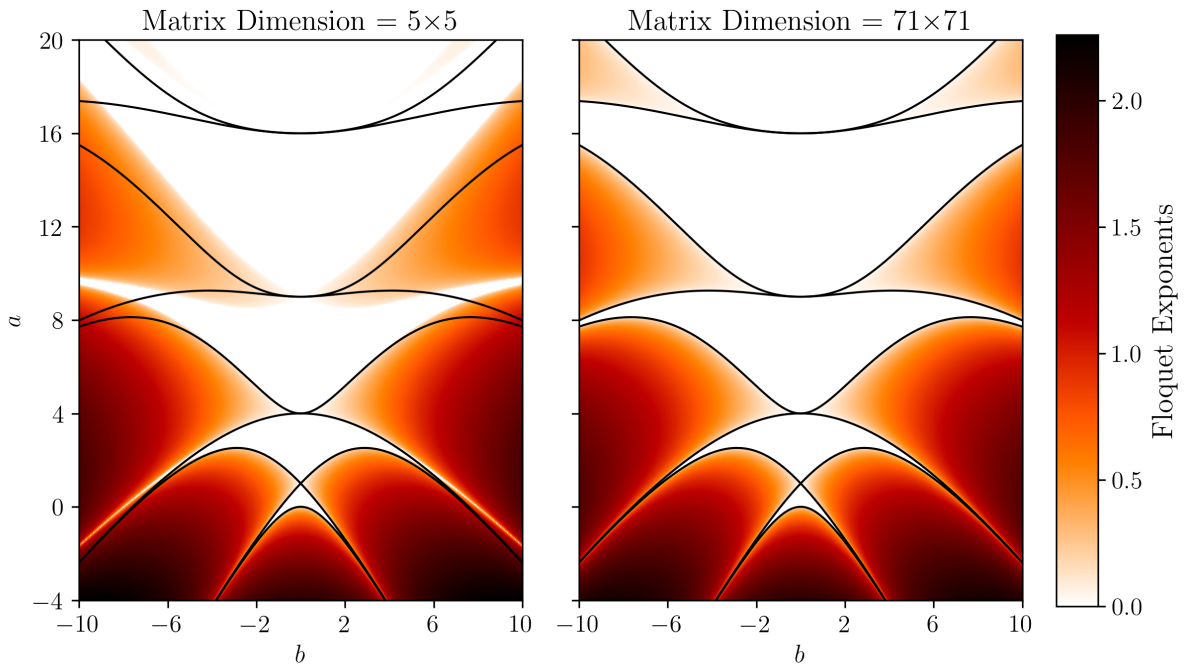


Figure 4.14: A more conventional view of the Mathieu stability chart calculated with the determinant of various sized matrices. The black lines across the charts are the correct values for the characteristic even and odd Mathieu equations. These lines should partition the Floquet exponents into stable and unstable regions, or white and coloured regions respectively with respect to my colour scheme. Clearly using a  $5 \times 5$  matrix results in a stability chart which is not partitioned correctly by the characteristic values, but using a  $71 \times 71$  matrix improves this.

# Chapter 5

## Conclusion

In this dissertation, we've investigated the Monodromy model as posed by [5], in particular how well its forth and sixth order Taylor approximations reproduce the resonant structure of the full Monodromy potential at  $\alpha \sim 1$  during preheating. We find that in all circumstances, the forth order potential may only superficially reproduce some of the structures of the Monodromy potential. Compared to the stability charts produced by the full Monodromy potential, those of the quartic potential has resonance bands in roughly the same location on the  $k\phi_0$  phase space with roughly similar shapes and roughly the same strength. Despite being similar, it is clear that the quadratic and forth order term alone is not sufficient to produce the finer details of those of the Monodromy potential. The sixth order potential reproduces the resonant structure better only for higher values of the parameter  $M$ ; for  $M \gg 1$  and  $\alpha > 1$ , this potential may even be sufficient when considering the stability of inflaton perturbations in the Monodromy model. When considering lower values of  $M$ , the sixth order term quickly losses its reproductive power as it dominates too much of the shape of the potential.

Regarding the quartic potential, we find that approximating inflaton perturbations as solutions to the Mathieu equation is accurate and precise. Resonance bands share the same shape and location, and are almost identical in size and strength. This is confirmed analytically.

## Appendix A

### More Comparisons

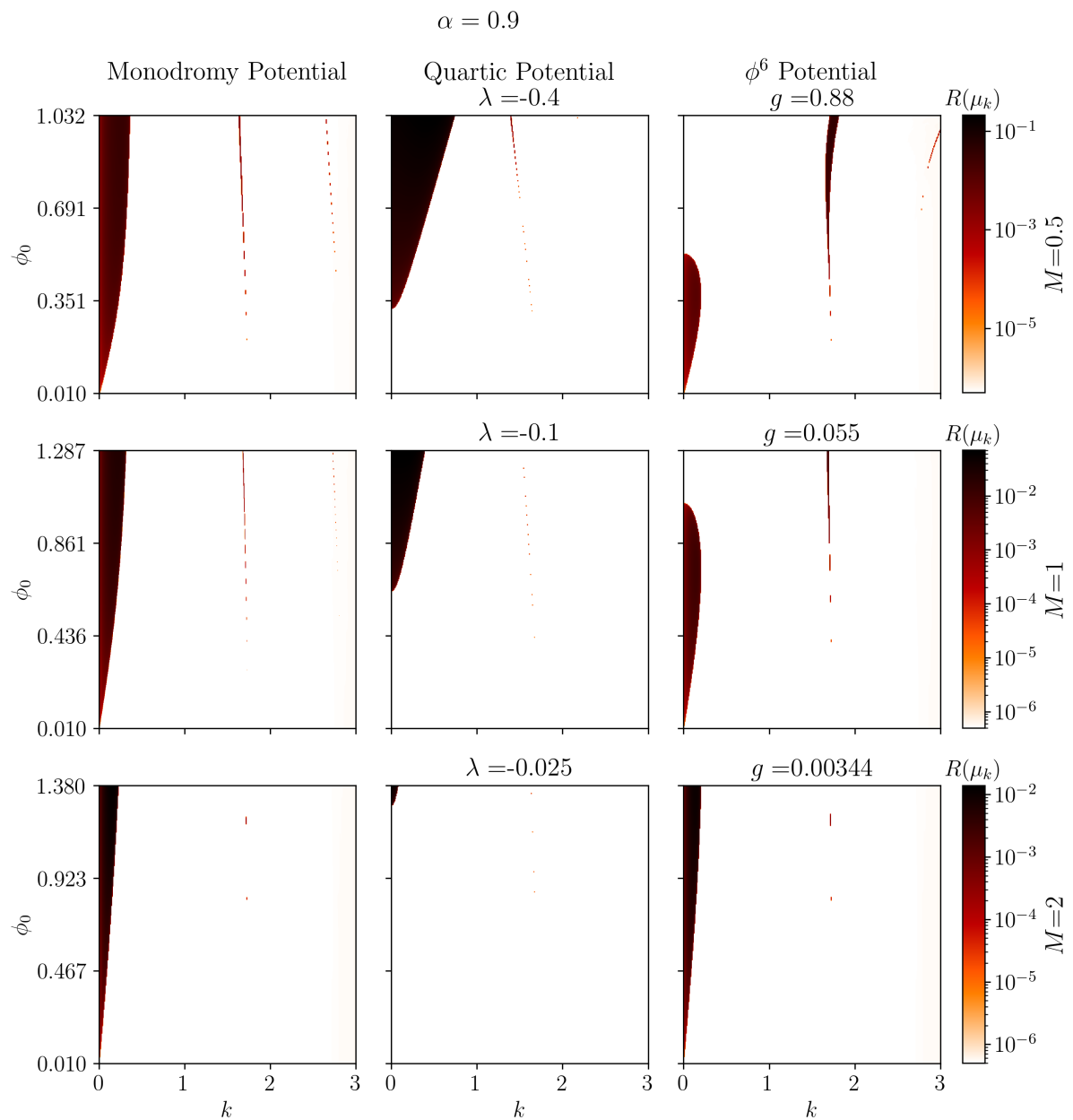


Figure A.1: Comparing the three potentials with  $\alpha = 0.9$  and varying  $M \in \{0.5, 1, 2\}$ .

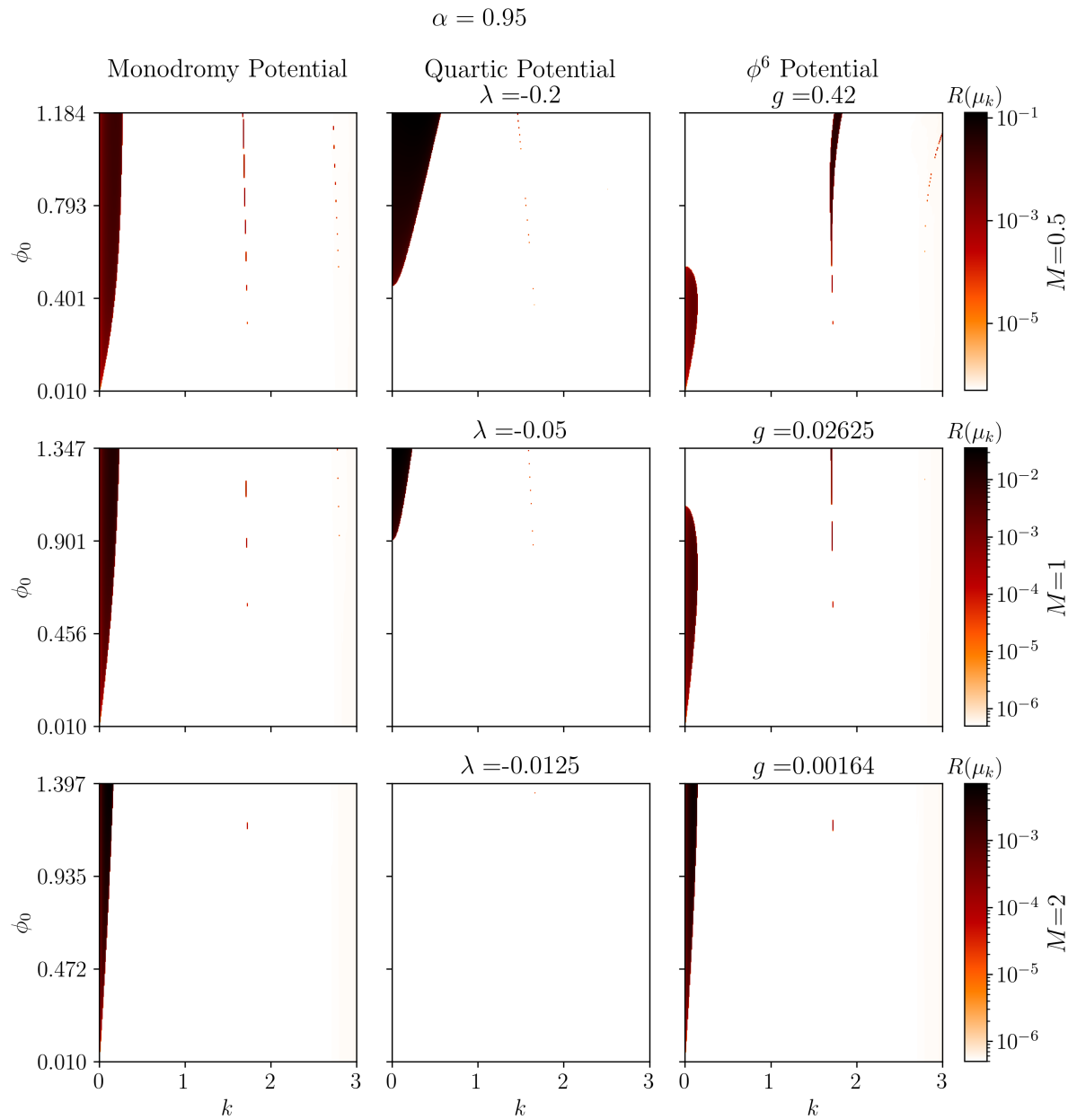


Figure A.2: Comparing the three potentials with  $\alpha = 0.95$  and varying  $M \in \{0.5, 1, 2\}$ .

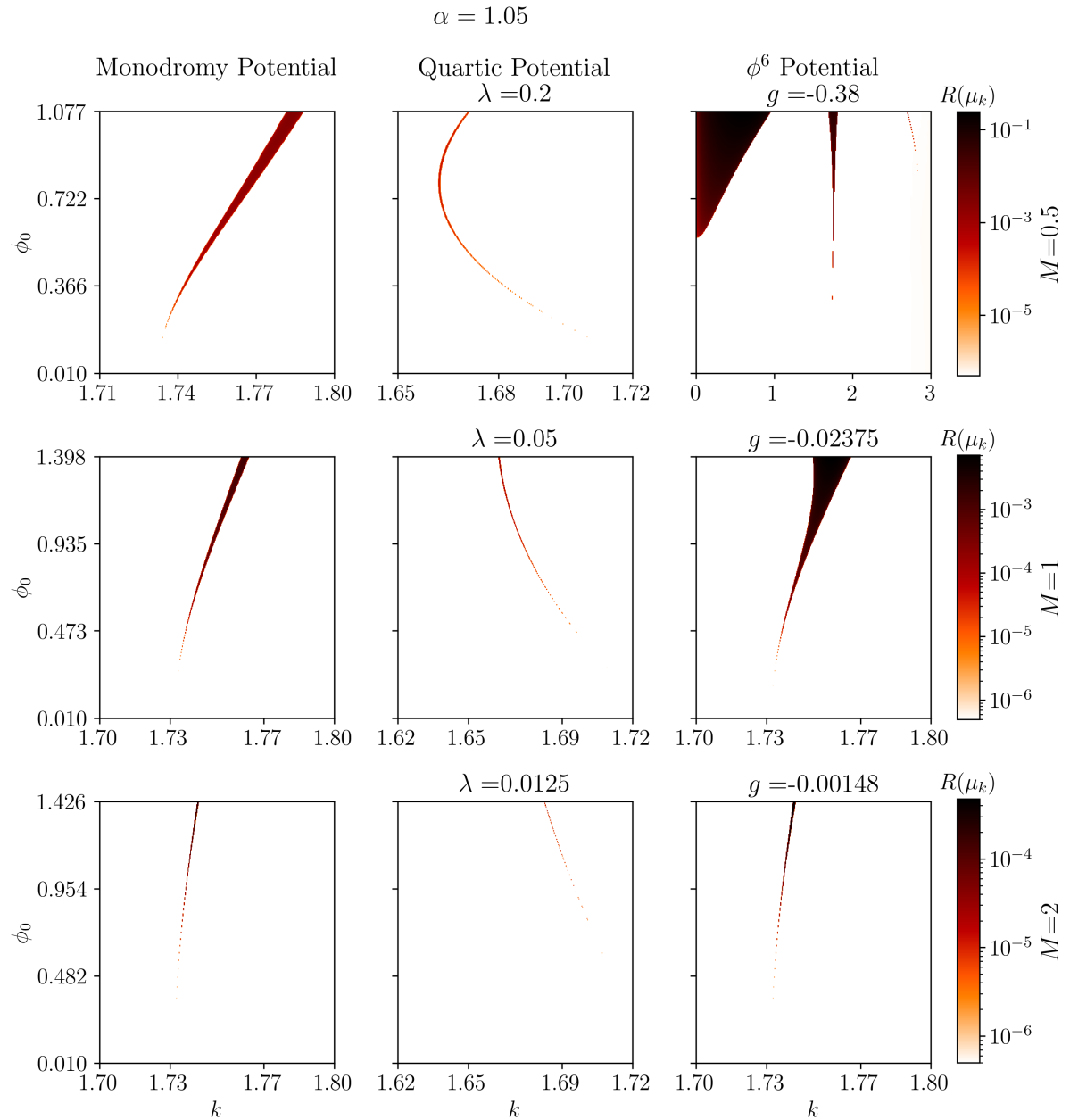


Figure A.3: Comparing the three potentials with  $\alpha = 1.05$  and varying  $M \in \{0.5, 1, 2\}$ , zoomed about first dominant resonance band.

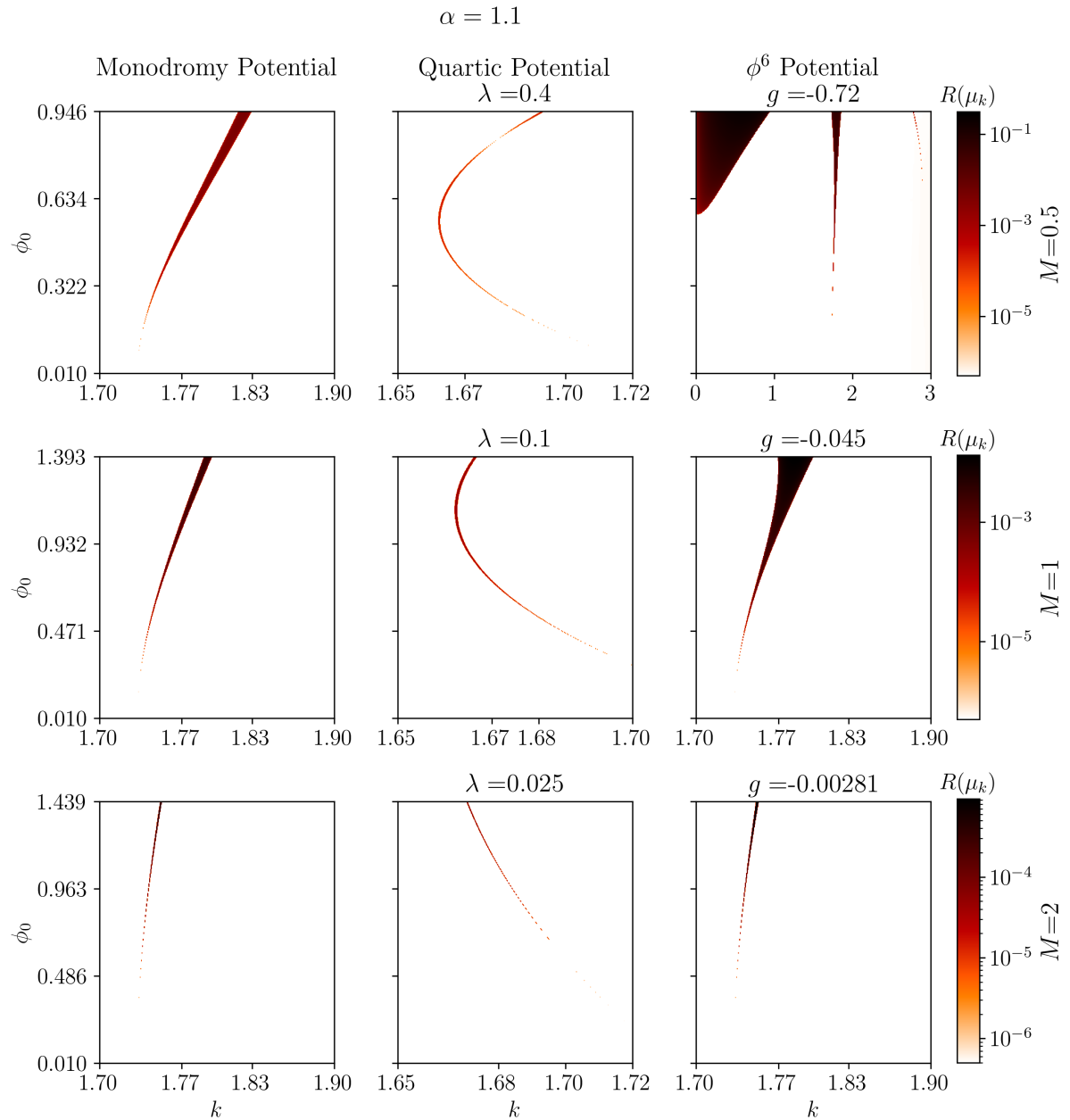


Figure A.4: Comparing the three potentials with  $\alpha = 1.1$  and varying  $M \in \{0.5, 1, 2\}$ , zoomed about first dominant resonance band.

## Appendix B

# $\phi^6$ Potential

Here, we examine the stability charts generated by the  $V_6(\phi)$  potential (equation 2.20) separately. The Floquet exponents are solved for by integrating equation 3.5 and using Floquet theory. With respect to the Monodromy model, valid expansions coefficients must obey  $\lambda > 0, g < 0$  or  $\lambda < 0, g > 0$ . I have plotted the stability charts for such coefficients for  $\lambda \in \{0.1, 0.01\}, g \in \{-0.1, -0.01, -0.001\}$  and  $\lambda \in \{-0.1, -0.01\}, g \in \{0.1, 0.01, 0.001\}$  in figures B.2 and B.3 respectively. For completeness, I have also plotted the stability charts for  $\lambda \in \{0.1, 0.01\}, g \in \{0.1, 0.01, 0.001\}$  and  $\lambda \in \{-0.1, -0.01\}, g \in \{-0.1, -0.01, -0.001\}$  in figures B.4 and B.5 respectively.

A class of potentials of interest are for larger  $g > 0$  (see first row of figures B.3 and B.4). The value of  $\phi_0$  which inflation ends is calculated by solving  $\epsilon(\phi_{\text{end}}) = 1$ ; usually  $\phi_{\text{end}} \sim 1.5$  using this method. However there exists threshold values of  $\lambda$  and  $g$  where  $\phi_{\text{end}}$  is calculated to be  $\sim 1.5$ , before discontinuously jumping to  $\sim 4$ , see figure B.1.

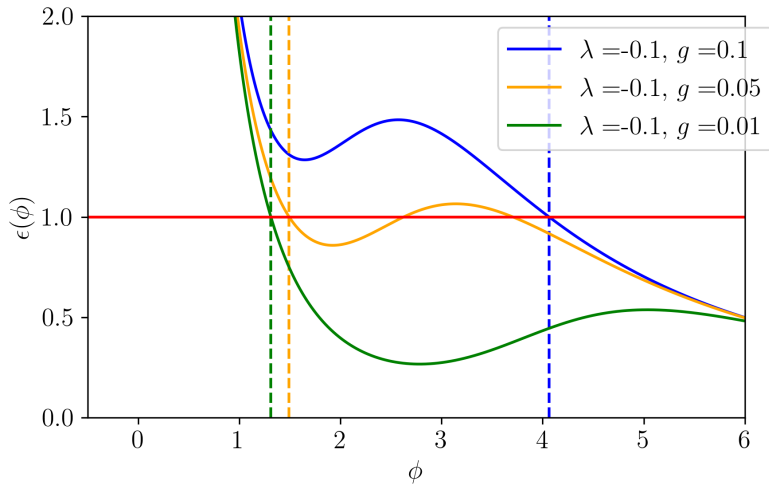


Figure B.1: The local minima of the slowroll parameter is below the value 1 for smaller  $g$ . The slowroll parameter increases for decreasing  $\phi$  hence crossing the value 1. For larger  $g$ , the local minima reaches above 1, hence there is no room for the slowroll parameter to pass 1 for lower  $\phi$ ; instead  $\phi_{\text{end}} \sim 4$ . Dashed lines mark the value of  $\phi_{\text{end}}$  found by solving  $\epsilon(\phi_{\text{end}}) = 1$ .

These higher values of  $\phi_{\text{end}}$  are outside of the range of  $\phi_0$  in the context of the sixth order Taylor term being a part of a Taylor approximation; truncating the range of  $\phi_0$  to end at  $\sim 1.5$  produces stability charts which are more in line with the other charts. Otherwise, there is not much of interest in higher  $g$  potentials.

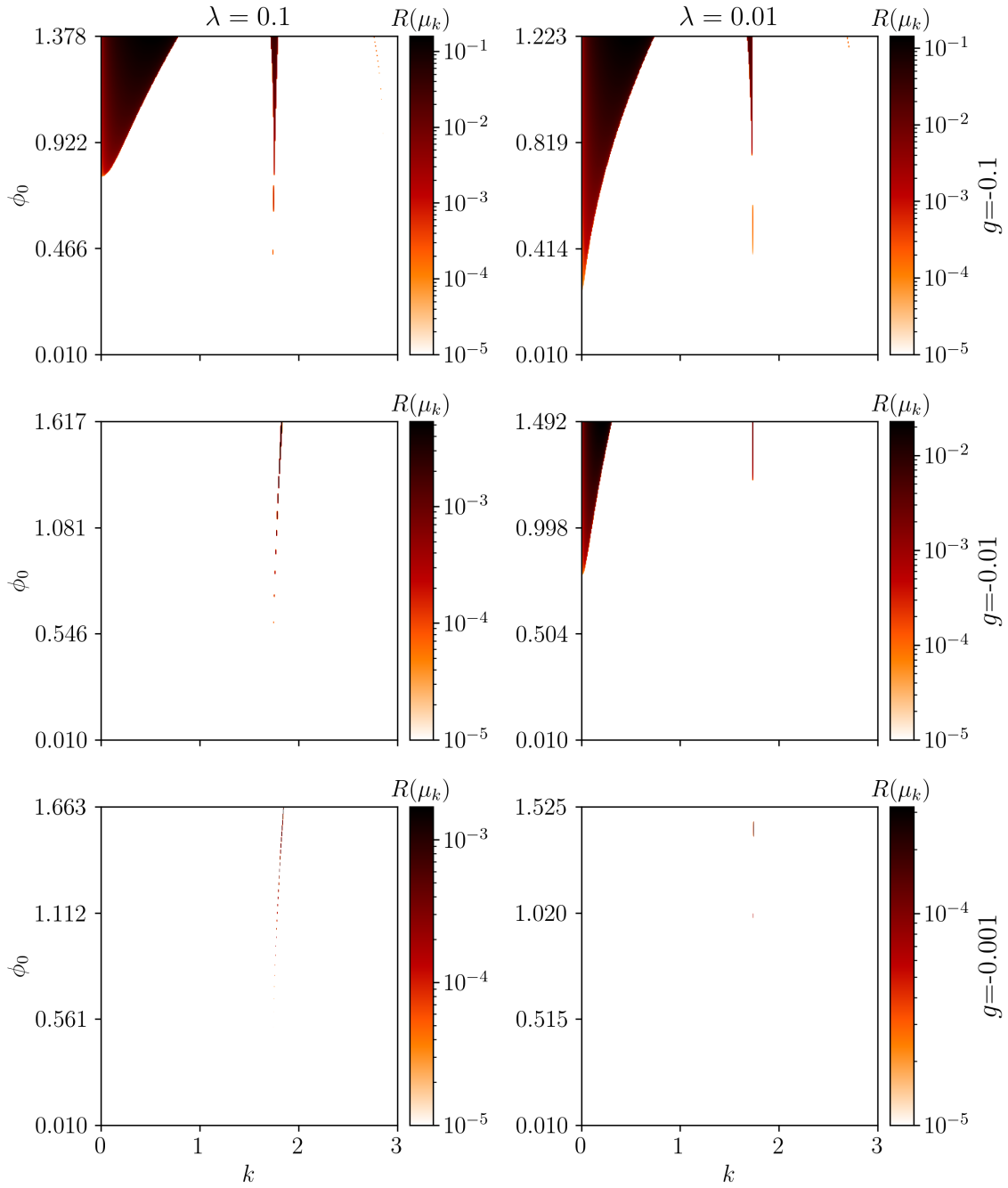


Figure B.2: Stability charts for the  $\phi^6$  potential for  $\lambda < 0$  and small  $g > 0$  for a range of  $k$  and  $\phi_0$  ranges from 0 to  $\phi_{\text{end}} + 0.1$ ,  $\phi_{\text{end}}$  solving  $\epsilon(\phi_{\text{end}})=1$ .

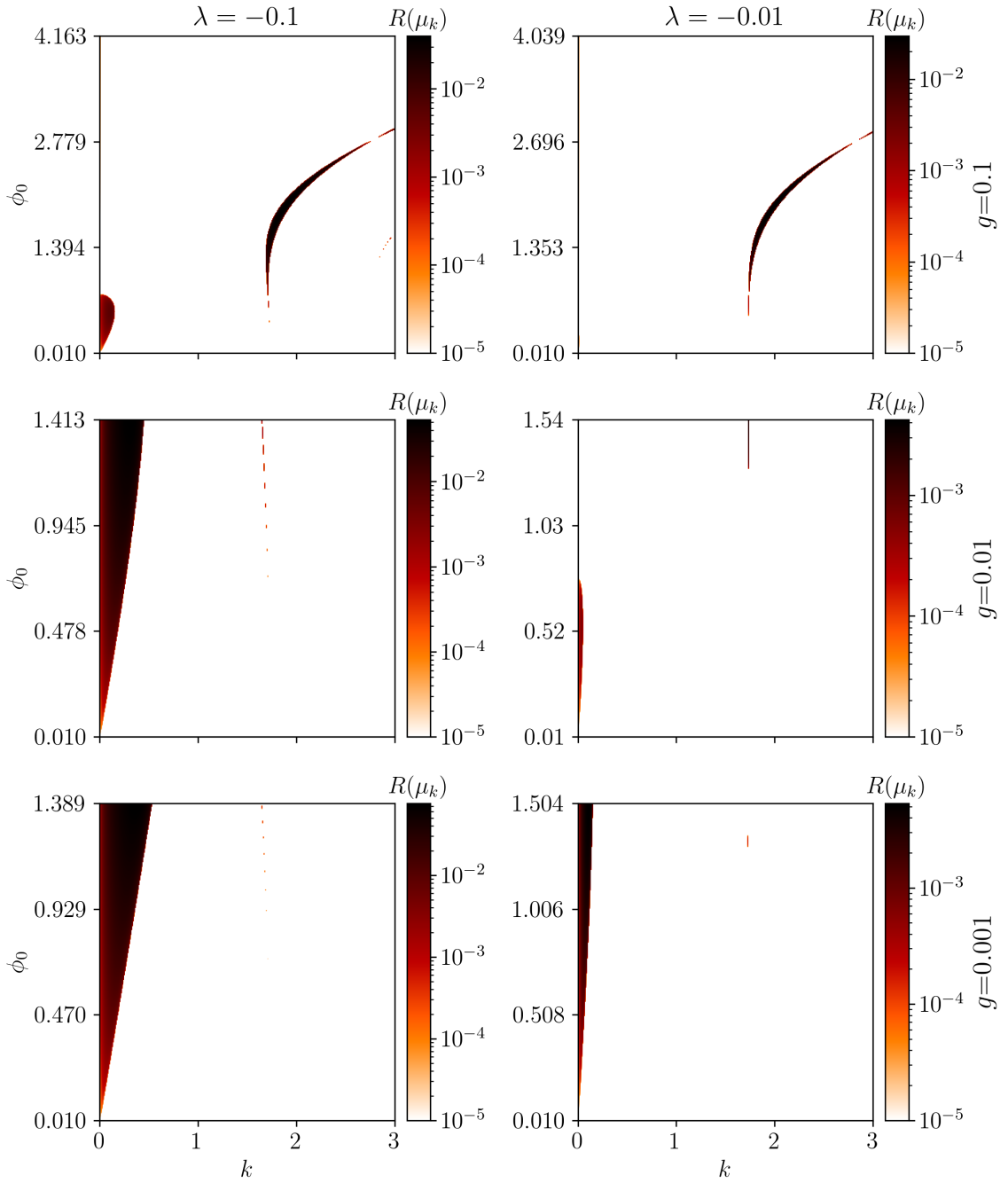


Figure B.3: Stability charts for the  $\phi^6$  potential for  $\lambda < 0$  and small  $g < 0$  for a range of  $k$  and  $\phi_0$  ranges from 0 to  $\phi_{\text{end}} + 0.1$ ,  $\phi_{\text{end}}$  solving  $\epsilon(\phi_{\text{end}})=1$ .

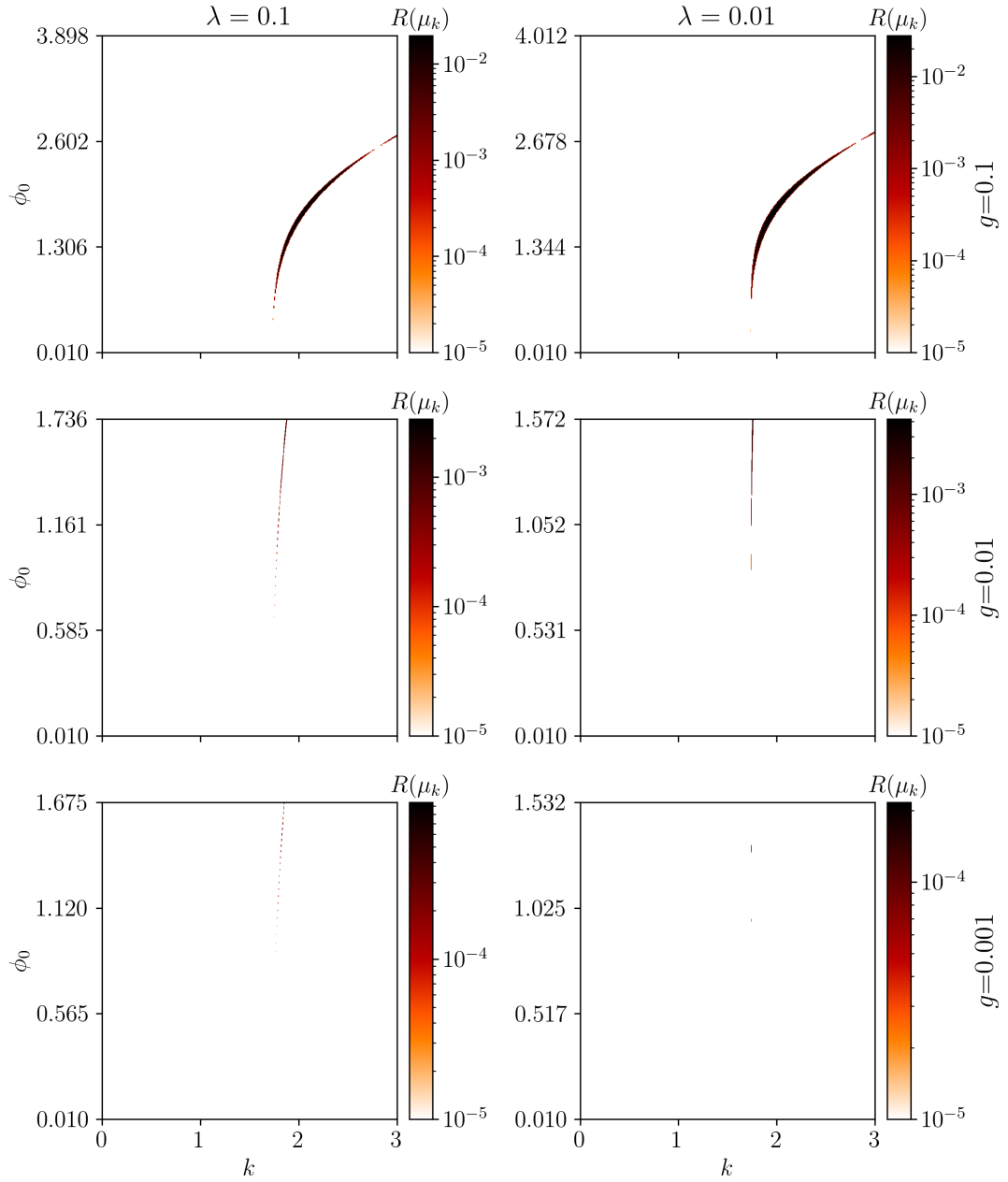


Figure B.4: Stability charts for the  $\phi^6$  potential for  $\lambda > 0$  and small  $g > 0$ . Where the resonance bands are too faint to see, they exists near  $k \sim 1.8$ .

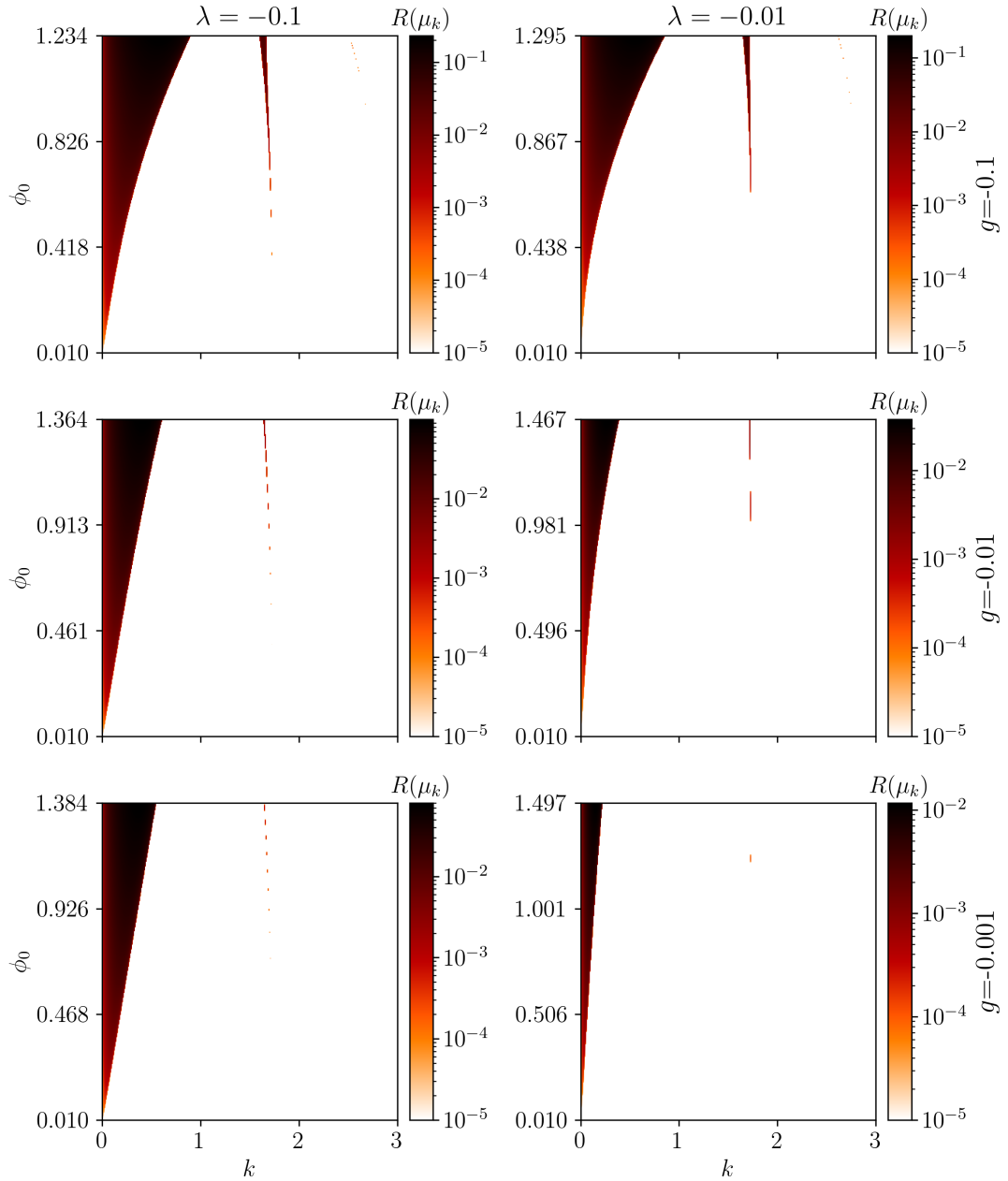


Figure B.5: Stability charts for the  $\phi^6$  potential for  $\lambda > 0$  and small  $g < 0$ . Where the resonance bands are too faint to see, they exists near  $k \sim 1.8$

# Bibliography

- [1] Barbara Ryden. Introduction to cosmology. 2003.
- [2] William H. Kinney. Tasi lectures on inflation, 2009.
- [3] Andrew R Liddle. An introduction to cosmological inflation. High energy physics and cosmology, page 260, 1998.
- [4] Alan H. Guth. Inflationary universe: A possible solution to the horizon and flatness problems. Phys. Rev. D, 23:347–356, Jan 1981. doi: 10.1103/PhysRevD.23.347. URL <https://link.aps.org/doi/10.1103/PhysRevD.23.347>.
- [5] Mustafa A. Amin, Richard Easther, Hal Finkel, Raphael Flauger, and Mark P. Hertzberg. Oscillons after inflation. Physical Review Letters, 108(24), Jun 2012. ISSN 1079-7114. doi: 10.1103/physrevlett.108.241302. URL <http://dx.doi.org/10.1103/PhysRevLett.108.241302>.
- [6] R. Grimshaw. Nonlinear Ordinary Differential Equations. CRC Press, 2017. ISBN 9781351428095. URL <https://books.google.co.nz/books?id=IFMPEAAAQBAJ>.
- [7] R. Reissig. Magnus, w. und s. winkler, hill's equation (interscience tracts in pure and applied mathematics, number 20). viii + 127 s. new york/london/sydney 1966. interscience publishers. preis geb. 68 s.net. ZAMM - Journal of Applied Mathematics and Mechanics / Zeitschrift für Angewandte Mathematik und Mechanik, 48(2):138–139, 1968. doi: <https://doi.org/10.1002/zamm.19680480218>. URL <https://onlinelibrary.wiley.com/doi/abs/10.1002/zamm.19680480218>.
- [8] Mustafa A. Amin, Phillip Zukin, and Edmund Bertschinger. Scale-dependent growth from a transition in dark energy dynamics. Physical Review D, 85(10), May 2012. ISSN 1550-2368. doi: 10.1103/physrevd.85.103510. URL <http://dx.doi.org/10.1103/PhysRevD.85.103510>.
- [9] Mustafa A. Amin, Mark P. Hertzberg, David I. Kaiser, and Johanna Karouby. Nonperturbative dynamics of reheating after inflation: A review. International Journal of Modern Physics D, 24(01):1530003, Dec 2014. ISSN 1793-6594. doi: 10.1142/s0218271815300037. URL <http://dx.doi.org/10.1142/S0218271815300037>.
- [10] Alvaro H. Salas and Jairo E. Castillo H. Exact solution to Duffing equation and the pendulum equation. Applied Mathematical Sciences, 8(176):8781–8789, 2014. doi: 10.12988/ams.2014.44243. URL <https://hal.archives-ouvertes.fr/hal-01356787>.
- [11] Roberto Coïsson, Graziano Vernizzi, and Xiaoke Yang. Mathieu functions and numerical solutions of the mathieu equation. pages 3–10, 09 2009. ISBN 978-1-4244-4452-6. doi: 10.1109/OSSC.2009.5416839.